Testing the ion-current model for flagellar length sensing and IFT regulation

Hiroaki Ishikawa[1], Jeremy Moore[2,†], Dennis R. Diener[3], Markus Delling[4], Wallace F. Marshall[1*]

1. Department of Biochemistry and Biophysics, University of California San Francisco, San Francisco, CA 94143
2. Kenyon College, Gambier, OH, 43022 and Summer Research Training Program at University of California San Francisco, San Francisco, CA 94143
3. Max Planck Institute of Molecular Cell Biology and Genetics, Dresden, Germany 01307
4. Department of Physiology, University of California San Francisco, San Francisco, CA 94143

*Corresponding author: Wallace F. Marshall
Address: UCSF Mail Code 2200
Genentech Hall Room N372F
600 16th St.
San Francisco, CA 94143
Phone: (415) 514-4304
Fax: (415) 502-4315
Email: wallace.marshall@ucsf.edu

† Present address
Department of Molecular Cellular and Developmental Biology, Yale University, New Heaven, CT 06511

Keywords
Cilia, flagella, intraflagellar transport, calcium

Abstract

Eukaryotic cilia and flagella are microtubule-based organelles whose relatively simple shape makes them ideal for investigating the fundamental question of organelle size regulation. Most of the flagellar materials are transported from the cell body via an active transport process called intraflagellar transport (IFT). The rate of IFT entry into flagella, known as IFT injection, has been shown to negatively correlate with flagellar length. However, it remains unknown how the cell measures the length of its flagella and controls IFT injection. One of the most-discussed theoretical models for length sensing to control IFT is the ion-current model, which posits that there is a uniform distribution of Ca^{2+} channels along the flagellum and that the Ca^{2+} current from the flagellum into the cell body increases linearly with flagellar length. In this model, the cell uses the Ca^{2+} current to negatively regulate IFT injection. The recent discovery that IFT entry into flagella is regulated by the phosphorylation of kinesin through a calcium-dependent protein kinase has provided further impetus for the ion-current model. To test this model, we measured and manipulated the levels of Ca^{2+} inside of *Chlamydomonas* flagella and quantified IFT injection. Although the concentration of Ca^{2+} inside of flagella was weakly correlated with the length of flagella, we found that IFT injection was reduced in calcium-deficient flagella, rather than increased as the model predicted, and that variation in IFT injection was uncorrelated with the occurrence of flagellar Ca^{2+} spikes. Thus, Ca^{2+} does not appear to function as a negative regulator of IFT injection, hence it cannot form the basis of a stable length control system.

Introduction

The mechanism by which cells control the size of organelles is a fundamental question in cell biology. Cells control the size of their organelles to efficiently use their energy and space (Chan and Marshall, 2012). However, it is mostly unknown how cells regulate organelle size, in part because the complexity of many organelles makes their size control mechanisms difficult to study. Eukaryotic cilia and flagella (we use these terms interchangeably) are an ideal model system to study size regulation because they consist of a simple, hair-like structure that can change in length while maintaining a constant diameter. Cilia and flagella are microtubule-based organelles that protrude from the cell body and are important for sensing extracellular signals and producing fluid flows (Ishikawa and Marshall, 2011; Reiter and Leroux, 2017). It is known that the length of cilia and flagella is cell type specific. For example, the biflagellate green alga *Chlamydomonas reinhardtii* adjusts the length of both flagella to a length suitable for swimming (Bauer et al., 2021; Bottier et al., 2019). If the flagella are too long or too short, the cells cannot swim efficiently. When flagella are removed from a cell, new flagella regenerate to the pre-severing length in around 90 min (Rosenbaum et al., 1969). Flagellar growth slows before they become full-length. This decelerating growth rate suggests that there is some mechanism that regulates the growth rate as a function of length.

Assembly and maintenance of flagella are dependent on an active transport system, intraflagellar transport (IFT). Because no protein synthesis occurs in the flagellum, new materials must be brought into the flagellum and carried to the site of assembly at the flagellar tip. IFT mediates this transport. IFT is carried out by huge protein complexes called trains, which have an elongate shape and move on the flagellar axoneme back and forth like a train (Jordan et al., 2018; Pigino et al., 2009). IFT trains assemble around the basal body and then enter the flagellum in a process known as IFT injection, after which they are carried to the flagellar tip by a heterotrimeric kinesin-2 motor and returned to the cell body by cytoplasmic dynein 2 (Ishikawa and Marshall, 2011; Rosenbaum and Witman, 2002). It is known that the rate of IFT injection is negatively correlated with the length of flagella during flagellar regeneration of (Engel et al., 2009;

83 Ludington et al., 2013), but it is unknown how cells regulate the rate of IFT injection. To
84 explain this negative correlation, several theoretical models have been proposed (Chan
85 and Marshall, 2012; Ludington et al., 2015; Rosenbaum, 2003).

86 One well-known model for the regulation of IFT injection is the ion-current model
87 (also known as the ciliary-current model). The ion-current model was first proposed by
88 Rosenbaum (2003) based on a previous electrophysiological study showing that voltage-
89 gated calcium channels were present in flagella at constant density (Beck and Uhl, 1994),
90 such that the number of voltage-gated calcium channels in the flagellum increases as the
91 flagellum elongates. Changes in flagellar calcium concentrations, due to changes in the
92 number and activity of calcium channels in the elongating flagella, were proposed to affect
93 calcium-dependent signaling pathways to regulate the rate of IFT injection or microtubule
94 assembly (Rosenbaum, 2003). In fact, changes in external Ca^{2+} are known to change
95 flagellar length in *Chlamydomonas* (Lefebvre et al., 1978; Quader et al., 1978; Tuxhorn
96 et al., 1998). The calcium ion-current model was first proposed based on physiological
97 measurements, but at the time, the molecular identity of the voltage-gated calcium
98 channel in the flagellar membrane was not known. More recently, several calcium channel
99 proteins have been shown to localize on the *Chlamydomonas* flagellum (Fujiu et al., 2011,
100 2009; Huang et al., 2007; Pazour et al., 2005). CAV2 is a subunit of a voltage-gated
101 calcium channel which resides in the flagellar membrane (Fujiu et al., 2009). The *ppr2*
102 mutant has a mutation in the CAV2 gene and is defective in the photophobic response
103 (Fujiu et al., 2009; Matsuda et al., 1998). TRP channels are also found in *Chlamydomonas*
104 flagella (Fujiu et al., 2011; Huang et al., 2007).

105 In the original ion-current model, it was not specified how Ca^{2+} contributes to
106 flagellar length regulation, but a potential molecular mechanism has been proposed by
107 Pan and colleagues (Liang et al., 2014, 2018). They found that a subunit of heterotrimeric
108 kinesin that drives IFT anterograde motion, FLA8/KIF3B, is phosphorylated by a calcium-
109 dependent protein kinase (CDPK1), and this phosphorylation negatively regulates IFT
110 injection into flagella. Because this work provides a potential missing link in understanding
111 the ion-current model, calcium-mediated regulation of IFT entry has increasingly been
112 viewed as a likely means of regulating IFT in response to flagellar length (Engelke et al.,

113 2019; Jiang et al., 2019; Kumari and Ray, 2022; Lechtreck et al., 2017; Liang et al., 2018).
114 There is thus a pressing need to test whether this model does in fact account for IFT
115 regulation as a function of length. The ion-current model hinges on two critical
116 assumptions (Figure 1A), both of which are experimentally testable. First, the amount of
117 flagellar Ca^{2+} needs to be an increasing function of the flagellar length. This assumption
118 would allow Ca^{2+} to serve as a length indicator within the ion-current model. Second, for
119 the ion-current model to work, cellular Ca^{2+} must negatively regulate IFT injection or
120 assembly of the axoneme. This is because if the amount of flagellar Ca^{2+} increases with
121 the flagellar length, it must work as a negative regulator to control the length of flagella in
122 order to have a stable length control system with negative feedback. If Ca^{2+} positively
123 regulated IFT injection, it could not be part of a stable feedback control loop and would
124 instead produce positive feedback.
125 Here, we tested the two underlying assumptions of the ion-current model by
126 quantitatively measuring the Ca^{2+} concentration inside of *Chlamydomonas* flagella using
127 a genetically encoded calcium biosensor, together IFT injection, in wild-type and calcium-
128 channel deficient flagella. The amount of Ca^{2+} inside of flagella was indeed correlated
129 with the length of flagella, as the model requires. However, IFT injection was reduced in
130 calcium-deficient flagella, rather than increased as the model predicted. Moreover, $CaCl_2$-
131 treated cells increased the amount of flagellar Ca^{2+} and IFT injection. We then examined
132 fluctuations of IFT at the time scale of individual injection events and compared these
133 fluctuations to fluctuations in flagellar Ca^{2+} and found no correlation, suggesting that
134 flagellar Ca^{2+} does not influence IFT injection at a short timescale. Thus, flagellar Ca^{2+}
135 apparently does not work as a negative regulator of IFT injection and therefore could not
136 form the basis of a stable length control system. These observations are thus inconsistent
137 with the ion-current model.
138

Results

Model for the ion-current model using kinesin phosphorylation

Before testing the calcium-based model experimentally, we first asked whether it could provide a stable length control mechanism, even in theory. We constructed a simplified model for flagellar length dynamics assuming that calcium entry is proportional to the flagellar length and that kinesin-2 activity is regulated by phosphorylation mediated by CDPK1 as previously reported (Liang et al., 2014) and summarized in Figure 1B. Details of this model, which integrates IFT-mediated transport, Ca^{2+} influx, and CDPK activity modulating IFT entry, are provided in Materials and Methods. As shown in Figure 1C, this model is able to produce a stable length control system, such that when flagella are removed they grow back to the correct length with decelerating kinetics that resemble those seen in actual flagella. Figure 1D further shows that the relative level of phosphorylation of kinesin changes during regeneration, smoothly increasing as the length increases, consistent with the experimental observations reported by Liang et al (2014). We note that this is a highly simplified model, and detailed numerical comparison to experiments is not useful since a number of parameters have unknown values. Nevertheless, this model serves to confirm the intuition that Ca^{2+} influx proportional to flagellar length, combined with CDPK-mediated regulation of IFT injection could, at least in principle, serve as a length control mechanism.

Quantitative flagellar Ca^{2+} detection using GCaMP

The first assumption of the ion-current model that we explore is the requirement that the Ca^{2+} amount in the flagellum should be an increasing function of flagellar length. To measure the amount of Ca^{2+} in *Chlamydomonas* flagella, we constructed *Chlamydomonas* strains that express GCaMP, a genetically encoded calcium indicator (Nakai et al., 2001), anchored in its flagella. GCaMP was fused to the C-terminus of dynein regulatory complex 4 (DRC4), an axonemal protein (Rupp and Porter, 2003), and DRC4-GCaMP was expressed in the *pf2-4* mutant cells, a loss-of-function mutant of DRC4. DRC4-GCaMP was localized along the length of flagella (Figure 2A) and rescued

169 the defective flagellar motility phenotype of the *pf2-4* mutant. DRC4 is a component of the
170 Nexin-Dynein Regulatory Complex, which is a part of the 96-nm axonemal repeat,
171 periodical structures on the axoneme (Heuser et al., 2009; Rupp and Porter, 2003).
172 Therefore, the amount of DRC4-GCaMP is constant per unit length, and the total quantity
173 of DRC4-GCaMP associated with axonemes is determined solely by the length of the
174 flagella. We previously showed that the amount of axonemal proteins, such as FAP20
175 and RSP3, is constant per unit length using GFP (Ishikawa et al., 2022). This result means
176 that our system using DRC4-GCaMP should be able to quantitatively detect flagellar Ca^{2+}.
177 To confirm that axonemal DRC4-GCaMP produces a signal that depends
178 quantitatively on free Ca^{2+}, we measured the GCaMP intensity using isolated DRC4-
179 GCaMP axonemes. We isolated flagella from DRC4-GCaMP (or DRC4-mCherry-
180 GCaMP) cells and removed the membrane from flagella so that Ca^{2+} can access the
181 axoneme-associated DRC4-GCaMP (or DRC4-mCherry-GCaMP). Isolated axonemes
182 were observed in various concentrations of free Ca^{2+} solutions (Figure 2B) and the
183 intensity was quantified (Figure 2C). GCaMP fluorescence showed a sigmoidal curve with
184 respect to free Ca^{2+} concentration, with an approximately linear response in the range of
185 free Ca^{2+} from 0.05 to 1 μM. Figure 2C provides a calibration curve that lets us
186 quantitatively measure Ca^{2+} in *Chlamydomonas* flagella based on DRC4-GCaMP
187 fluorescence.
188
189 **The Ca^{2+} influx into the flagellum is correlated with flagellar length**
190 To check whether the amount of Ca^{2+} influx into the flagellum is increased with increasing
191 flagellar length, we observed DRC4-GCaMP in flagella of living cells using total internal
192 reflection fluorescence (TIRF) microscopy during flagellar regeneration. *Chlamydomonas*
193 flagella were amputated with the pH shock method (see Materials and Methods), allowing
194 us to measure Ca^{2+} influx as a function of flagellar length as the flagella regrow. We
195 observed intensity fluctuation of GCaMP in live cells, indicating the presence of Ca^{2+} influx
196 (Figure 3A and Video 1). This intensity fluctuation was not observed when 1 mM EGTA
197 was added to the media (~150 nM of free Ca^{2+}, which is the same level as the cytosolic

198 Ca^{2+} concentration; Figure 3A and Video 3). This result indicated that most of the Ca^{2+}
199 influx came from outside of the cell.

200 TIRF movies of DRC4-GCaMP were converted into kymographs to measure the
201 calcium amount in the flagellum (Figure 3A). The amount of flagellar Ca^{2+} influx was
202 significantly correlated with the flagellar length but with a broad distribution of values
203 around the trend line (Figure 3B, Pearson correlation coefficient $\rho = 0.33$, and coefficient
204 of determination $r^2 = 0.11$). Longer flagella generally allowed more Ca^{2+} influx but also
205 had greater variability. This variability is mainly caused by the fact that the Ca^{2+} influx
206 does not occur consistently. The frequency of flagellar Ca^{2+} influx events (spikes) was not
207 correlated with the flagellar length (Figure 3C, $\rho = 0.14$, and $r^2 = 0.02$). The pattern of
208 Ca^{2+} influx events varied from flagellum to flagellum and from time to time and did not
209 match a Poisson distribution (Figure 3 - figure supplements 1and 2). Consistent with
210 previous reports, the Ca^{2+} influx into the flagellum was compartmentalized, such that
211 there was no correlation in Ca^{2+} influx events between the two flagella from the same cell
212 (Figure 3A, Figure 3 - figure supplement 1, and Video 1; Collingridge et al., 2013).

213 To reduce the Ca^{2+} influx into the flagellum, we used a calcium channel mutant
214 strain, *ppr2* (Fujiu et al., 2009; Matsuda et al., 1998). The *ppr2* mutant has an insertion in
215 the CAV2 gene, which encodes a voltage-gated calcium channel localized to flagella
216 (Fujiu et al., 2009). In the *ppr2* mutant, we still observed Ca^{2+} influx events, but the amount
217 of Ca^{2+} influx was no longer correlated with the flagellar length (Figure 3B, $\rho = 0.09$, and
218 $r^2 = 0.02$) and the magnitude of the influx was smaller than control on the average (Figure
219 3D). Interestingly, the *ppr2* mutant reduced Ca^{2+} influx most strongly at the distal region
220 of flagella (Figure 3A). This reduction is presumably caused by the loss of CAV2 protein,
221 which localizes in the distal part of the flagellum (Fujiu et al., 2009). Conversely, we tried
222 to increase the amount of flagellar Ca^{2+} by raising the concentration of extracellular Ca^{2+}.
223 When 1 mM $CaCl_2$ was added to the media, we confirmed that the amount of flagellar
224 Ca^{2+} was increased (Figures 3 A, B, and D). Thus, we could regulate the amount of
225 flagellar Ca^{2+} by using the flagellar Ca^{2+} channel mutant cells or changing the external
226 Ca^{2+} concentration.
227

228 **IFT injection was reduced in calcium-deficient flagella**

229 As discussed above, in order for the ion-current model to work, Ca^{2+} would need to be a
230 negative regulator of IFT injection. Any reduction in Ca^{2+} influx should thus lead to
231 increased IFT injection. Because the amount of Ca^{2+} influx into flagella was reduced in
232 the *ppr2* mutant (Figures 3 B and D), IFT injection in the *ppr2* mutant should be increased
233 compared to control cells if the ion-current model is correct. To test this prediction, we
234 quantified the IFT injection using kinesin-associated protein (KAP), which is a subunit of
235 the heteromeric kinesin-2 motor (IFT kinesin), tagged with green fluorescent protein
236 (GFP). We focused on the kinesin-2 motor because this is the component of IFT that is
237 apparently regulated by Ca^{2+} (Liang et al., 2018, 2014). KAP-GFP was expressed in the
238 *fla3* mutant, which has a point mutation in the *FLA3* gene (encodes KAP), and rescued
239 the phenotype of the *fla3* mutant (Mueller et al., 2005). This *fla3* KAP-GFP strain was also
240 used in previous studies for measuring IFT injection intensity (Engel et al., 2009; Ishikawa
241 and Marshall, 2017; Ludington et al., 2013). Movies of KAP-GFP were converted into
242 kymographs to measure IFT injection (Figure 4A and Videos 4-6). Similar to previous
243 reports (Ishikawa and Marshall, 2017; Ludington et al., 2013), the injection intensity of
244 KAP-GFP decreases as flagellar length increases in control cells (Figure 4B). In the *ppr2*
245 mutant, IFT injection was also negatively correlated with the flagellar length but was
246 reduced in short flagella compared to control cells (Figure 4 B and C). This is the opposite
247 of the prediction of the ion-current model. To confirm that flagellar Ca^{2+} is related to this
248 IFT reduction phenotype, we treated KAP-GFP cells with 1 mM EGTA and measured the
249 intensity of IFT injection. EGTA treated cells showed reduced, rather than increased, IFT
250 injection, similar to that seen in *ppr2* mutant cells (Figure 4 B and C). In contrast, the KAP-
251 GFP cells treated with 1 mM $CaCl_2$ increased the intensity of IFT injection (Figure 4 B and
252 C). Because reduction in Ca^{2+} caused a decrease, rather than an increase in IFT injection
253 and vice versa, these results suggested that flagellar Ca^{2+} does not work as a negative
254 regulator of IFT injection. Our observations thus do not support the ion-current model.
255

256 **Effect of Ca^{2+} on flagellar regeneration and disassembly**

257 The preceding results were based on quantifying KAP entry into flagella. As an alternative
258 indicator of IFT based on IFT function, we note that IFT is thought to drive flagellar
259 elongation, such that increased IFT injection should lead to faster flagellar growth, while
260 decreased IFT injection should lead to slower growth. Flagellar growth can thus be used
261 as an indicator of functionally altered IFT injection. To confirm our result that flagellar Ca^{2+}
262 does not inhibit IFT injection as predicted by the ion-current model, we performed flagellar
263 regeneration assays while altering Ca^{2+} concentrations. *Chlamydomonas* cells were
264 treated with low-pH media to remove their flagella and cultured with TAP media with or
265 without 1 mM EGTA (free Ca^{2+} in the two types of media is 149.3 nM and 170 μM,
266 respectively). 150 nM free Ca^{2+} is comparable to the cytosolic Ca^{2+} concentration but was
267 enough to eliminate detectable flagellar Ca^{2+} influx (Figure 3A and Video 3). 1 mM EGTA
268 treated cells showed slower flagellar regeneration than control cells but could eventually
269 reach the original length of flagella (Figure 5A, orange triangles). This observation is
270 consistent with previous studies (Liang and Pan, 2013) but is contrary to the prediction of
271 the ion-current model, in which reduction of calcium should lead to faster regeneration
272 due to increased IFT injection.

273 These findings suggested that at least a cytoplasmic concentration of Ca^{2+} is
274 enough for flagellar regeneration, and further Ca^{2+} influx into the flagellum is not essential.
275 Interestingly, the *ppr2* mutant cells showed slower flagellar regeneration and shorter final
276 length than 1 mM EGTA treated cells even though the *ppr2* mutants still have some Ca^{2+}
277 influx events (Figure 5A, red square). In any case, Ca^{2+} influx through CAV2 is apparently
278 not necessary for assembly of flagella, and CAV2 might have another role for flagellar
279 assembly or maintenance. To investigate whether extracellular Ca^{2+} can promote flagellar
280 assembly, we added 1 mM $CaCl_2$ to TAP media after pH shock. Flagellar regeneration
281 kinetics in $CaCl_2$ added media did not change relative to normal TAP media (Figure 5A,
282 green diamonds). The extra amount of extracellular Ca^{2+} does not help assembly of
283 flagella. Because the IFT injection was increased in the $CaCl_2$ treated cells, without
284 causing an increase in flagellar assembly, these IFT trains might carry less cargo, such
285 as tubulin. It has been reported that tubulin loading onto IFT trains is regulated by flagellar
286 length (Craft et al., 2015).

287 While flagellar Ca^{2+} does not seem to affect either IFT injection or flagellar
288 assembly in the way expected from the ion-current model, an alternative length control
289 model involving Ca^{2+} could be that flagellar Ca^{2+} might promote flagellar disassembly,
290 such that longer flagella would experience a faster disassembly rate. We therefore tested
291 how flagellar Ca^{2+} affects flagellar disassembly using the temperature-sensitive *fla10*
292 mutant cells (Huang et al., 1977). The *fla10* mutant cells gradually reduce their flagellar
293 length at the restrictive temperature (Huang et al., 1977; Marshall et al., 2005). The *ppr2*
294 mutation had no clear effect on disassembly rates, and EGTA treated cells showed faster
295 disassembly kinetics than untreated cells in both control and *ppr2* mutant cells (Figure
296 5B), rather than the slower kinetics that would be predicted if flagellar Ca^{2+} normally
297 promoted disassembly. We also tested putative mutations in flagella-localized calcium
298 pumps and found no effect on flagellar length (Figure 5 - figure supplement 1). Overall,
299 our results suggest that flagellar Ca^{2+} does not inhibit IFT injection or flagellar assembly
300 or promote flagellar disassembly.
301
302 **Flagellar Ca^{2+} does not change IFT injection even at short timescales**
303 Our analyses suggested that flagellar Ca^{2+} helps flagellar assembly and maintenance
304 rather than flagellar disassembly and does not inhibit IFT injection. However, this
305 conclusion is based on separate measurements of Ca^{2+} and IFT carried out under
306 identical conditions but not in the same cells, and is based on comparison of population
307 averages as a function of length, leaving open the possibility that there could be
308 correlations between Ca^{2+} influx and IFT injection over short periods of time. Such a short
309 time scale correlation might be important given that calcium shows spiking dynamics that
310 are more regularly spaced than predicted by a Poisson distribution. These spikes could
311 play a role in transiently delaying or shifting the time at which IFT injections occur, leading
312 to a more regular or uniform IFT time series. To ask how flagellar Ca^{2+} might contribute
313 to flagellar length control or IFT injection over short time scales in individual flagella, we
314 performed dual-channel live-cell imaging of Ca^{2+} and IFT using DRC4-GCaMP and
315 mScarlet-IFT54 (Figure 6A and Video 9). IFT injection measured in dual-channel imaging
316 was negatively correlated with flagellar length, similar to our KAP-GFP analysis (Figure

317 6B). Both frequency and speed of anterograde mScarlet-IFT54 showed a similar
318 distribution with KAP-GFP (Figures 4D, 4E, 6C, and 6D). Likewise, GCaMP intensity
319 measured in dual-channel imaging also showed a similar distribution as previously seen
320 in our single-wavelength imaging (Figure 6E). However, there was no obvious correlation
321 between Ca^{2+} influx and IFT injection (Figure 6F), consistent with our results above
322 comparing separate single-channel imaging data.

323 To further investigate the potential effect of Ca^{2+} influx on IFT behavior on a short
324 time scale, we asked whether a burst of Ca^{2+} influx might cause a transient change in IFT
325 behavior. We selected kymograph regions in which there was no observed Ca^{2+} influx for
326 at least 10 s before a Ca^{2+} burst and analyzed successive 5 s intervals (Figure 7A). In
327 this analysis, we did not find a statistically significant difference in intensity or frequency
328 of IFT injection during the time windows before or after Ca^{2+} influx (Figure 7 B and C).
329 However, average speeds of both anterograde and retrograde IFT appeared to increase
330 during Ca^{2+} influx. The increase in average speed was due to the fact that paused IFT
331 trains, which had an initial speed of zero, became re-activated during the Ca^{2+} bursts,
332 consistent with a previous report (Collingridge et al., 2013; Fort et al., 2021). In
333 experiments in which cells were treated with 1 mM EGTA, a slowdown of IFT trains was
334 also observed (Figure 4E). Moreover, the background intensity of the mScarlet-IFT54
335 channel decreased after Ca^{2+} influx (Figure 7I). This background reduction means that
336 IFT trains, which paused and accumulated during the prolonged absence of Ca^{2+} influx,
337 restarted with Ca^{2+} influx. Because most of the pausing IFT trains were retrograde IFT,
338 the intensity of the returning IFT was transiently increased after Ca^{2+} influx (Figure 7C).
339 This result showed that Ca^{2+} bursts can clear out the accumulated retrograde IFT trains
340 from flagella. Additional examples are given in Figure 7 - figure supplement 1. Because
341 a portion of IFT trains, after returning to the base, can be reused as new anterograde IFT
342 trains (Wingfield et al., 2017), we expected that IFT injection might increase after a burst
343 of Ca^{2+} influx, due to the resulting release of paused retrograde trains. However, IFT
344 injection did not obviously increase after the returning IFT trains reached the base of the
345 flagellum in this time range (Figure 7B). Together, these results indicate that Ca^{2+} influx
346 can restart paused IFT trains and increase the amount of returning IFT trains to the base

347 of flagella, but that IFT injection is not controlled by Ca^{2+} influx in a short time and is not
348 triggered by a transient increase in the arrival of retrograde trains.

Discussion

The role of Ca^{2+} dependent phosphorylation in IFT

The work of Liang et al. (2014) has clearly shown that the IFT kinesin is regulated by CDPK1. Why then in our hands do we not observe the expected effect of calcium channel modulation and Ca^{2+} depletion on length? For one thing, it has not been shown directly that this kinase requires Ca^{2+} for its activity in *Chlamydomonas*. CDPK1 has also been shown to regulate IFT turnaround at the flagellar tip (Liang et al., 2014), however recent studies showed that IFT can turn around at the tip without Ca^{2+} (Chien et al., 2017; Nievergelt et al., 2022). Thus, Ca^{2+} might not be required for the activation of CDPK1. Furthermore, it is important to note that regulation does not have to imply feedback control. We modeled the phosphorylation of kinesin as occurring in response to Ca^{2+} entering through the flagellar membrane, which is consistent with the original ion-current model (Rosenbaum, 2003). However, it is also possible that the phosphorylation is regulated by cytoplasmic Ca^{2+} fluctuations, which could be independent of the flagellum, thus constituting a separate regulatory input. In such a scenario, CDPK1 would not be part of a feedback loop because it would not be sensitive to flagellar length. This case may therefore be similar to the length-regulating kinase LF4 in *Chlamydomonas*. Null mutants in *lf4* have flagella that are approximately double the normal length, but their length is still regulated in the sense that length variation is constrained (Bauer et al., 2021). Since length is still regulated in a null mutant of *lf4*, the kinase cannot be part of a feedback loop essential for length control. Instead, it is likely to carry information from other signaling pathways to alter the set-point of flagellar length. We speculate that the calcium-dependent regulation of kinesin entry into flagella during IFT may provide a way for cellular states, such as cell cycle or metabolic state, to influence flagellar length, and not as a feedback control loop necessary for length regulation *per se*. Liang and Pan (2013) also showed that another calcium-dependent protein kinase, CDPK3, helps flagellar assembly at low Ca^{2+} concentrations. CDPK1 and CDPK3 may have opposite regulation over length control downstream of Ca^{2+}. We speculate that regulation of some flagella related processes by cytoplasmic, rather than flagellar Ca^{2+}, may explain the long-known

379 result that reduction in Ca^{2+} leads to shortening or loss of flagella (Lefebvre et al., 1978)
380 which has always stood in contradiction to the ion-current model.
381
382 **The role of flagellar Ca^{2+} influx in flagellar length control**
383 The ion-current model assumed that the Ca^{2+} influx was stable. However, the amount of
384 flagellar Ca^{2+} was highly dispersed around the trend line although on average it is
385 correlated with flagellar length. This variability mostly came from the randomness of the
386 Ca^{2+} influx events. However, the Ca^{2+} influx events did not match a Poisson distribution,
387 consistent with the idea of Ca^{2+} bursting. Ca^{2+} influx may itself be regulated by some other
388 process. A previous study found that increased Ca^{2+} influx is evoked in the trailing
389 flagellum during gliding motility (Collingridge et al., 2013). Because our cells were also
390 mounted on glass surfaces to image flagella, the gliding motility could also be one source
391 of variation in our experiments. Because we imaged cells embedded in agarose, they
392 were prevented from gliding extensively. Previous studies have also shown that poly-
393 lysine-coated coverslips can increase Ca^{2+} influx events in flagella (Fort et al., 2021).
394 These findings suggested that a mechanical stimulus on the flagellum is one of the
395 triggers of Ca^{2+} influx. The difference in Ca^{2+} influx between the two flagella might also
396 be related to the phototactic behavior of *Chlamydomonas*. *Chlamydomonas* cells can
397 change beat frequency and beat pattern of each flagellum to turn towards the light source
398 (Rüffer and Nultsch, 1991), and they are controlled by Ca^{2+} (Kamiya and Witman, 1984).
399 This phototactic response is mediated by the signal transduction from the photoreceptor,
400 which is located at the eyespot (Harz and Hegemann, 1991). Because these kinds of Ca^{2+}
401 responses are dependent on the specific local environment in which the cell might find
402 itself, they are unlikely to produce a stable signal, making them less useful as an indicator
403 of flagellar length.
404 The flagellar regeneration kinetics of 1 mM EGTA treated cells (Figure 5A) were
405 similar to results reported in rapamycin treated *Chlamydomonas* cells. Rapamycin
406 treated cells also showed slower flagella regeneration kinetics, but the length of the
407 flagellum eventually reached its original length before deflagellation (Yuan et al., 2012).
408 Rapamycin inhibits the mTOR pathway (Wullschleger et al., 2006), and it is known that

409 intracellular Ca^{2+} is necessary for the activation of the mTOR pathway (Gulati et al., 2008;
410 Li et al., 2016). The slow regeneration kinetics of EGTA treated cells might be caused by
411 the inhibition of the cytoplasmic mTOR pathway. Other calcium dependent processes in
412 the cytoplasm might also potentially affect IFT, and our results cannot rule out this
413 possibility. However, we note that the ppr2 mutant also fails to show the effect on IFT or
414 regeneration predicted by the ion current model.

415 It has been proposed that not only IFT injection, but also cargo loading onto IFT
416 particles, is regulated as a function of flagellar length (Craft et al., 2015). Quantitative
417 studies show that some or all of this apparent length-dependent cargo loading is a result
418 of the fact that in longer flagella, IFT trains are shorter and thus have fewer tubulin binding
419 sites (Wemmer et al., 2020). Nevertheless, the question arises whether flagellar Ca^{2+}
420 could play a role in regulating tubulin binding to the IFT particles. If this was the case,
421 Ca^{2+} would have to inhibit cargo binding, in order for cargo binding to decrease at longer
422 lengths as has been reported. Reduction of flagellar Ca^{2+} should thus lead to increased
423 cargo binding, causing flagella to grow faster and/or to longer lengths. Our measurements
424 of flagellar growth rate (Figure 5A) show that in fact the opposite is true.

425 Taken together, our experimental test of the ion-current model for flagella length
426 control appears to rule out an ion channel model based on Ca^{2+} influx into flagella. It is
427 formally possible that some other ion might serve as a length sensor, but thus far Ca^{2+} is
428 the only candidate ion for which a plausible mechanistic link to IFT regulation has been
429 reported.

430 We previously provided experimental evidence against two other potential length
431 control models - an "initial bolus" model (Ludington et al., 2015) in which IFT particles are
432 initially injected into a newly formed flagellum but then recycle without being able to leave,
433 as well as a "time-of-flight" model (Ishikawa and Marshall, 2017; Ludington et al., 2015)
434 in which IFT particles contain a molecular timer that tracks the time spent inside the
435 flagellum as a proxy for flagellar length. Here we rule out a calcium-based ion-current
436 model for length sensing as well. Of the models we have considered, the remaining model
437 for length-dependent IFT regulation is one based on diffusive return of the IFT kinesin
438 (Hendel et al., 2018). The experiments presented here do not address this diffusion-

439 based model, which is thus far the only model for which there is no opposing experimental
440 evidence.
441
442 **Return of re-activated retrograde trains**
443 When anterograde IFT trains reach the tip, they remodel into a different number of
444 retrograde trains (Chien et al., 2017). Much less is known about possible remodeling of
445 retrograde trains at the basal body in order to re-inject them. One possibility might be that
446 some of returning IFT particles are immediately packaged into anterograde trains and re-
447 injected back into the same flagellum (Wingfield et al., 2017).
448 We observed the re-activation of large paused retrograde trains by Ca^{2+} spikes,
449 which has been reported to occur due to an ability of Ca^{2+} influx to break the link between
450 IFT and membrane proteins and thus restart paused retrograde IFT trains (Fort et al.,
451 2021). We note in addition that many cytoplasmic dynein cargo adaptors contain EF hand
452 domains (Reck-Peterson et al., 2018), and at least in the case of CRACR2a it has been
453 shown that increased cellular calcium can activate dynein motility (Wang et al., 2019).
454 Regardless of the mechanism, the re-activation of these paused trains results in the
455 sudden return of a large quantity of IFT particles to the base, as visualized by a strong
456 retrograde trace. However, when we then looked at the anterograde trains entering the
457 flagellum in a short time period after the return of these trains, no significant increase in
458 IFT injection was observed (Figure 7). This observation implies that returning IFT particles
459 are not directly re-injected. This may indicate that the remodeling/recycling of retrograde
460 IFT trains into anterograde IFT trains simply needs more time, or it might be because IFT
461 injection is controlled by some other process that determines the timing of new particle
462 injection, regardless of instantaneous retrograde return events.
463

464 **Materials and methods**
465

466 ***Chlamydomonas* strains and culture condition**

467 *Chlamydomonas reinhardtii* strains, wild-type 137c (CC-125), the *fla3-1* mutant
468 expressing KAP-GFP (CC-4296)(Mueller et al., 2005), the *fla10-1* mutant (CC-
469 1919)(Huang et al., 1977), and the *pf2-4* mutant (CC-4404)(Rupp and Porter, 2003) were
470 obtained from the Chlamydomonas Resource Center (University of Minnesota, St. Paul,
471 MN). The *ppr2* mutant strain was provided by Kenjiro Yoshimura (Fujiu et al., 2009;
472 Matsuda et al., 1998). The *ift54-2* mutant strain expressing mScarlet-IFT54 was provided
473 by Karl Lechtreck (Fort et al., 2021; Wingfield et al., 2017). The generation of *pf2-1* DRC4-
474 GCaMP has been described (Nievergelt et al., 2022). The presence of mutant alleles was
475 confirmed by PCR. *pf2-1* DRC4-GCaMP was crossed with the *pf2-4* mutant. We crossed
476 the *pf2-4* DRC4-GCaMP strain with the *ppr2* strain to generate the *ppr2 pf2-4* double
477 mutant strain expressing DRC4-GCaMP. We generated the *ppr2* mutant expressing KAP-
478 GFP by crossing the *ppr2* mutant with the KAP-GFP strain. For dual-channel imaging of
479 Ca^{2+} and IFT, we crossed the *pf2-4* DRC4-GCaMP strain with *ift54-2* mScarlet-IFT54
480 strain to generate the *pf2-4 ift54-2* double mutant strain expressing both DRC4-GCaMP
481 and mScarlet-IFT54. For flagellar disassembly assays, the *fla10-1* mutant strain was
482 crossed with the *ppr2* strain to generate the *fla10-1 ppr2* double mutant strain.
483 *Chlamydomonas* cells were grown in liquid Tris-acetate-phosphate (TAP) medium media
484 (20 mM Tris HCl, 3.5 mM NH_4Cl, 0.2 mM $MgSO_4$, 0.17 mM $CaCl_2$, 1 mM K_3PO_4, and
485 1000× diluted Hutner's trace elements, titrated to pH 7.0 with glacial acetic acid) (Harris
486 et al., 2009) at room temperature with constant aeration in light.
487

488 **Flagellar regeneration and disassembly assays**

489 Flagellar regeneration assays were performed in the same manner as previously
490 described (Ishikawa and Marshall, 2017). Briefly, *Chlamydomonas* liquid cultures were
491 adjusted to pH 4.5 by adding 0.5 M acetic acid and incubated for 1 min to amputate
492 flagella, and then the pH was returned to pH 7.0 with 0.5 M KOH. The pH shocked cells
493 were pelleted by centrifugation and resuspended with fresh TAP media with or without 1

494 mM EGTA (free Ca^{2+} is 149.3 nM and 170 μM, respectively). For the flagellar disassembly
495 assay, we used the *fla10* temperature-sensitive kinesin mutant. The *fla10* mutant and
496 *fla10 ppr2* double mutant cells were cultured in TAP media at room temperature for one
497 day and then 1 mM EGTA was added, after which the cultures were transferred to a 33ºC
498 incubator with continuous illumination. Cells were fixed with 2.5% glutaraldehyde before
499 and at time points after pH shock or temperature shift. Fixed cells were imaged by
500 differential interference contrast (DIC) microscopy using an inverted microscope
501 (AxioVert 200M, Zeiss, Jena, Germany) with an air objective (Plan Apo 40x/NA 0.75,
502 Zeiss) and a CCD camera (Axiocam MRm, Zeiss). The lengths of 20 biflagellated cells at
503 each time point and each sample were measured using ImageJ (NIH, Bethesda, MD).
504 We often observed the *fla10* mutant and *fla10 ppr2* double mutant cells with a single
505 flagellum after the temperature shift but measured only the cells with two flagella. We did
506 not observe any *fla10 ppr2* double mutant cells with two flagella at 300 min after the
507 temperature shift.
508
509 **Live-cell imaging**
510 All live-cell imaging was performed during the regeneration of flagella. *Chlamydomonas*
511 flagella were amputated by the pH shock method as described above. #1 (22 x 22 mm)
512 coverslips were coated with 0.1% poly-L-lysine solution (Sigma, St. Louis, MO) for 10 min
513 and washed three times with deionized water. A culture of flagella-regenerating cells was
514 placed on a poly-L-lysine-coated coverslip for 3 min and removed most of the media.
515 Then, the coverslip was mounted on glass slides with 2% agarose/TAP with or without 1
516 mM EGTA and sealed with VALAP (1:1:1 Vaseline, lanolin, and paraffin). Agarose
517 embedding prevents cells from gliding. Images were acquired on an inverted microscope
518 (Eclipse Ti-E, Nikon, Tokyo, Japan) configured for TIRF microscopy using an oil objective
519 (Apo TIRF 100 ×/NA 1.49; Nikon), MLC400 laser combiner with solid-state lasers of 405,
520 488, 561, and 647nm (Keysight, Santa Rosa, CA) and an electron-multiplying CCD (EM-
521 CCD; iXon Ultra 897, Andor, Belfast, UK) camera controlled with Nikon Elements
522 Software (v5.20.00 b1423). Image sequences were continuously acquired using triggered
523 acquisition using the 488 nm and/or 561 nm lasers (4.0 mW and 1.6 mW, respectively)

524 and single band-pass (ET525/50m and ET600/60m, Chroma, Bellows Falls, VT) or dual
525 band-pass emission filters (59012m, Chroma) with a camera exposure of 50 ms and an
526 EM gain of 300 used for both channels.
527
528 **Quantifying axonemal DRC4-GCaMP**
529 To quantify the GCaMP reactivity, axonemes were isolated from the *pf2-4* DRC4-GCaMP
530 or *pf2-4* DRC4-mCherry-GCaMP strains. Flagellar isolation and demembranation were
531 performed as previously described (Wakabayashi and Kamiya, 2015). For Ca^{2+} titrations,
532 GCaMP axonemes were washed and resuspended in 30 mM MOPS, pH 7.2, 100 mM KCl
533 with either 10 mM EGTA (zero free Ca^{2+}) or 10 mM CaEGTA (39 μM free Ca^{2+}) from the
534 calcium calibration buffer kit (Thermo Fisher, Waltham, MA) and then observed on the
535 TIRF microscope (Eclipse Ti-E, Nikon). GCaMP intensity was measured using ImageJ.
536 Each axoneme was traced by hand using the Segmented line tool with a 7-pixel line width,
537 analyzed by the Plot Profile function, and then average intensity per pixel was calculated.
538 At least 13 axonemes were analyzed for each calcium concentration.
539
540 **Imaging analysis**
541 For GCaMP intensity analysis, kymographs were generated from movies of DRC4-
542 GCaMP using ImageJ. GCaMP kymographs were analyzed in MATLAB (MathWorks,
543 Natick, MA). The kymographs were smoothed using a 2D Gaussian filter and
544 photobleach-corrected. The peak of Ca^{2+} influx was detected using the findpeaks function
545 on MATLAB. The intensity of Ca^{2+} influx was calculated as the sum of the peak area of
546 Ca^{2+} influx divided by imaging time.
547 For quantitative analysis of IFT injection and behavior, kymographs were
548 generated from movies of KAP-GFP or mScarlet-IFT54 using Kymograph Clear (Mangeol
549 et al., 2016). IFT trajectories were detected using KymoButler, a deep learning-based
550 software (Jakobs et al., 2019), and extracted as coordinates. IFT kymographs and
551 coordinates of IFT trajectories were analyzed in MATLAB. Whenever separated IFT
552 trajectories were detected on the same track, they were connected, and any overlaps of
553 IFT trajectories were removed. The IFT injection intensity was calculated as the total

554 intensity of anterograde IFT trajectories per unit length and unit time. IFT velocity and
555 frequency were calculated from extracted IFT trajectories. The intensities of IFT injection
556 and returning IFT were calculated as the sum of the average intensity of injecting or
557 returning IFT trajectories during the image acquisition period.

558 For analysis of dual-channel imaging, dual-channel movies were converted to
559 kymographs for each channel. The mScarlet channel showed slight bleed-through to the
560 GCaMP channel because we used the dual band-pass emission filter for imaging. To
561 remove the weak bleed-through of mScaret-IFT54 signals from DRC4-GCaMP
562 kymographs, 20% intensity of the mScaret-IFT54 kymograph was subtracted from the
563 GCaMP kymograph. The intensity of Ca^{2+} influx was calculated in the same manner as
564 described above. To investigate the short-term effect of Ca^{2+} influx on IFT, we selected
565 the kymographs without Ca^{2+} influx for more than 10 s before bundles of Ca^{2+} influx that
566 had more than 2,000 intensities. We calculated IFT injection, velocity, and frequency for
567 10 s and 15 s each before and after the start of the Ca^{2+} influx in these kymographs. The
568 intensities of IFT injection and returning IFT were calculated as the sum of the intensity
569 of IFT trajectories that started from or returned to the base within the time range. We also
570 calculated the background intensity from the kymographs which removed both
571 anterograde and retrograde IFT trajectories. All calculations were performed using
572 custom-written routines in MATLAB.

573 For statistical analyses and graph generation, we used GraphPad Prism
574 (GraphPad, San Diego, CA). The statistical significance of Ca^{2+} influx between the control
575 and the *ppr2* mutant was tested using an unpaired t test. Statistical significances of IFT
576 behaviors were tested using a paired t test.

577

578 **Computational model**

579 We constructed a computational model of flagellar length control based on the general
580 concept proposed by Rosenbaum (2003) and based on the biochemical work of Liang et
581 al on CDPK1 mediated phosphorylated of kinesin-2 (Liang et al., 2014). This model is
582 based on the following assumptions. First, as first proposed by Rosenbaum (Rosenbaum,
583 2003) based on the measurements of Beck and Uhl (Beck and Uhl, 1994), we assume

584 that the concentration of calcium at the base is on average proportional to the length of
585 the flagellum.
586
587 $$Ca^{2+} = \alpha L$$
588
589 Where α is a proportionality constant.
590 Second, we assume that CDPK1 activity depends on the instantaneous calcium
591 concentration according to a saturable binding relation with some dissociation constant
592 that is an adjustable parameter of the model. In effect, this assumption means that the
593 kinetics of allosteric regulation of CDPK1 activity by calcium occur on a much faster time
594 scale than the other events of our model. This yields the relation:
595
596 $$F_{CDPK} = \frac{\alpha L}{\alpha L + K_D}$$
597
598 Where F_{CDPK} is the fraction of enzyme that is active, and K_D is the dissociation constant
599 of calcium binding by CDPK1.
600 Third, we assume that phosphorylation of kinesin by CDPK1, as well as subsequent
601 dephosphorylation of kinesin, both take place on a fast timescale relative to the timescale
602 of flagellar length change, such that the fraction of active kinesin is at a quasi-state in the
603 model. Given this assumption, we represent the fraction of phosphorylated kinesin as a
604 function of the relative activity of CDPK1 according to a Michaelis-Menten equation:
605
606 $$K = 1 - \frac{F}{F + K_M}$$
607
608 Where K_M is the Michaelis constant for the interaction of the enzyme CDPK1 with the
609 kinesin substrate.
610 Fourth, based on the results of Liang et al (2014), we assume that the number of IFT
611 particles entering the flagellum per unit time is proportional to the fraction of non-

phosphorylated kinesin-2 proteins. Fifth, we assume that the occupancy of IFT particles for tubulin is proportional to the quantity of tubulin available in the cytoplasm, which is equivalent to saying that binding is not saturated. This was the assumption used in previous models (Marshall et al., 2005) and is consistent with observations on the fractional occupancy of tubulin during flagellar assembly (Craft et al., 2015; Wemmer et al., 2020). We thus represent the available tubulin pool as (P-2L) where P is the total precursor (tubulin) pool and L is the length of each of the two flagella. With these assumptions, we can describe flagellar length dynamics as follows:

$$\frac{dL}{dt} = A * K * (P - 2L) - D$$

Where A is a proportionality constant describing the total pool of kinesins, such that AK is the pool of kinesins currently active, as well as the incremental increase in length that occurs when a kinesin delivers cargo to the tip. D is the rate of disassembly, which is assumed to be constant based on prior measurements (Marshall et al., 2005).

The net growth rate is used to update the length using the Euler method with a timestep of 0.02 seconds. Output values are stored every 50 timesteps (1 second of simulation). Source codes of the model and data analyses used in this work (Ishikawa and Marshall 2022) can be found here:

https://github.com/ishikawaUCSF/IonCurrentModel

Acknowledgements

The authors thank current and past members of the Marshall laboratory as well as Joel Rosenbaum and Xin Xiang for helpful discussions; DeLaine Larsen, Kari Herrington, SoYeon Kim and the Nikon Imaging Center at UCSF for microscopy resources and assistance; and Karl Lechtreck (University of Georgia) and Kenjiro Yoshimura (Shibaura Institute of Technology) for generously sharing *Chlamydomonas* strains. This work was supported by NIH grants R35GM130327 (W.F.M.) and R01GM130908 (M.D).

Abbreviations

CDPK: calcium-dependent protein kinase

DIC: differential interference contrast

DRC: dynein regulatory complex

GFP: green fluorescent protein

IFT: intraflagellar transport

KAP: kinesin-associated protein

TIRF: total internal reflection fluorescence

Note: This is a preprint and is not peer reviewed

Declaration of Competing Interests

The authors declare that they have no competing interests.

657 **References**

658

659 Bauer D, Ishikawa H, Wemmer KA, Hendel NL, Kondev J, Marshall WF. 2021. Analysis
660 of biological noise in the flagellar length control system. *iScience* **24**:102354.
661 doi:10.1016/j.isci.2021.102354

662 Beck C, Uhl R. 1994. On the localization of voltage-sensitive calcium channels in the
663 flagella of Chlamydomonas reinhardtii. *J Cell Biol* **125**:1119–1125.

664 Bottier M, Thomas KA, Dutcher SK, Bayly PV. 2019. How Does Cilium Length Affect
665 Beating? *Biophys J* **116**:1292–1304. doi:10.1016/j.bpj.2019.02.012

666 Chan Y-HM, Marshall WF. 2012. How cells know the size of their organelles. *Science*
667 **337**:1186–1189. doi:10.1126/science.1223539

668 Chien A, Shih SM, Bower R, Tritschler D, Porter ME, Yildiz A. 2017. Dynamics of the
669 IFT machinery at the ciliary tip. *eLife* **6**:e28606. doi:10.7554/eLife.28606

670 Collingridge P, Brownlee C, Wheeler GL. 2013. Compartmentalized calcium signaling in
671 cilia regulates intraflagellar transport. *Curr Biol* **23**:2311–2318.
672 doi:10.1016/j.cub.2013.09.059

673 Craft JM, Harris JA, Hyman S, Kner P, Lechtreck KF. 2015. Tubulin transport by IFT is
674 upregulated during ciliary growth by a cilium-autonomous mechanism. *J Cell Biol*
675 **208**:223–237. doi:10.1083/jcb.201409036

676 Engel BD, Ludington WB, Marshall WF. 2009. Intraflagellar transport particle size scales
677 inversely with flagellar length: revisiting the balance-point length control model. *J*
678 *Cell Biol* **187**:81–89. doi:10.1083/jcb.200812084

679 Engelke MF, Waas B, Kearns SE, Suber A, Boss A, Allen BL, Verhey KJ. 2019. Acute
680 inhibition of heterotrimeric kinesin-2 function reveals mechanisms of
681 intraflagellar transport in mammalian cilia. *Curr. Biol.* **29**:1137-1148. e4.
682 doi:10.1016/j.cub.2019.02.043

683 Fort C, Collingridge P, Brownlee C, Wheeler G. 2021. Ca2+ elevations disrupt
684 interactions between intraflagellar transport and the flagella membrane in
685 Chlamydomonas. *J Cell Sci* **134**:jcs253492. doi:10.1242/jcs.253492

686 Fujiu K, Nakayama Y, Iida H, Sokabe M, Yoshimura K. 2011. Mechanoreception in
687 motile flagella of Chlamydomonas. *Nat Cell Biol* **13**:630–632.
688 doi:10.1038/ncb2214
689 Fujiu K, Nakayama Y, Yanagisawa A, Sokabe M, Yoshimura K. 2009. Chlamydomonas
690 CAV2 encodes a voltage- dependent calcium channel required for the flagellar
691 waveform conversion. *Curr Biol* **19**:133–139. doi:10.1016/j.cub.2008.11.068
692 Gulati P, Gaspers LD, Dann SG, Joaquin M, Nobukuni T, Natt F, Kozma SC, Thomas
693 AP, Thomas G. 2008. Amino acids activate mTOR complex 1 via Ca2+/CaM
694 signaling to hVps34. *Cell Metab* **7**:456–465. doi:10.1016/j.cmet.2008.03.002
695 Harris EH, Stern DB, Witman GB, editors. 2009. Chapter 8 - Chlamydomonas in the
696 Laboratory The Chlamydomonas Sourcebook (Second Edition). London:
697 Academic Press. pp. 241–302. doi:10.1016/B978-0-12-370873-1.00008-3
698 Harz H, Hegemann P. 1991. Rhodopsin-regulated calcium currents in Chlamydomonas.
699 *Nature* **351**:489–491. doi:10.1038/351489a0
700 Hendel NL, Thomson M, Marshall WF. 2018. Diffusion as a Ruler: Modeling Kinesin
701 Diffusion as a Length Sensor for Intraflagellar Transport. *Biophys J* **114**:663–674.
702 doi:10.1016/j.bpj.2017.11.3784
703 Heuser T, Raytchev M, Krell J, Porter ME, Nicastro D. 2009. The dynein regulatory
704 complex is the nexin link and a major regulatory node in cilia and flagella. *J Cell*
705 *Biol* **187**:921–933. doi:10.1083/jcb.200908067
706 Huang B, Rifkin MR, Luck DJ. 1977. Temperature-sensitive mutations affecting flagellar
707 assembly and function in Chlamydomonas reinhardtii. *J Cell Biol* **72**:67–85.
708 Huang K, Diener DR, Mitchell A, Pazour GJ, Witman GB, Rosenbaum JL. 2007.
709 Function and dynamics of PKD2 in Chlamydomonas reinhardtii flagella. *J Cell*
710 *Biol* **179**:501–514. doi:10.1083/jcb.200704069
711 Ishikawa H, Marshall WF. 2017. Testing the time-of-flight model for flagellar length
712 sensing. *Mol Biol Cell* **28**:3447–3456. doi:10.1091/mbc.E17-06-0384
713 Ishikawa H, Marshall WF. 2011. Ciliogenesis: building the cell's antenna. *Nat Rev Mol*
714 *Cell Biol* **12**:222–234. doi:10.1038/nrm3085

715 Ishikawa H, Tian JL, Yu JE, Marshall WF, Qin H. 2022. Biosynthesis of Linear Protein
716 Nanoarrays Using the Flagellar Axoneme. *ACS Synth Biol* **11**:1454–1465.
717 doi:10.1021/acssynbio.1c00439
718 Ishikawa H, Marshall WF. 2022. IonCurrentModel. *Github*.
719 https://github.com/ishikawaUCSF/IonCurrentModel c916c61
720 Jakobs MA, Dimitracopoulos A, Franze K. 2019. KymoButler, a deep learning software
721 for automated kymograph analysis. *eLife* **8**:e42288. doi:10.7554/eLife.42288
722 Jiang YY, Maier W, Baumeister R, Minevich G, Joachimiak E, Wloga D, Ruan Z, Kannan N,
723 Bocarro S, Bahraini A, Vasudevan KK, Lechtreck K, Orias E, Gaertig J. 2019.
724 LF4/MOK and a CDK-related kinase regulate the number and length of cilia in
725 Tetrahymena. *PLoS Genet*. **15**:e1008099 doi:10.1371/journal.pgen.1008099
726 Jordan MA, Diener DR, Stepanek L, Pigino G. 2018. The cryo-EM structure of
727 intraflagellar transport trains reveals how dynein is inactivated to ensure
728 unidirectional anterograde movement in cilia. *Nat Cell Biol* **20**:1250–1255.
729 doi:10.1038/s41556-018-0213-1
730 Kamiya R, Witman GB. 1984. Submicromolar levels of calcium control the balance of
731 beating between the two flagella in demembranated models of Chlamydomonas.
732 *J Cell Biol* **98**:97–107. doi:10.1083/jcb.98.1.97
733 Kumari D, Ray K. 2022. Phosphoregulation of kinesins involved in long-range
734 intracellular transport. *Front Cell Dev Biol*. **10**:873164.
735 doi:10.3389/fcell.2022.873164
736 Lechtreck KF, Van De Weghe JC, Harris JA, Liu P. 2017. Protein transport in growing
737 and steady-state cilia. *Traffic* **18**:277–286. doi:10.1111/tra.12474
738 Lefebvre PA, Nordstrom SA, Moulder JE, Rosenbaum JL. 1978. Flagellar elongation
739 and shortening in Chlamydomonas. IV. Effects of flagellar detachment,
740 regeneration, and resorption on the induction of flagellar protein synthesis. *J Cell*
741 *Biol* **78**:8–27. doi:10.1083/jcb.78.1.8
742 Li R-J, Xu J, Fu C, Zhang J, Zheng YG, Jia H, Liu JO. 2016. Regulation of mTORC1 by
743 lysosomal calcium and calmodulin. *eLife* **5**:e19360. doi:10.7554/eLife.19360

744 Liang Y, Pan J. 2013. Regulation of flagellar biogenesis by a calcium dependent protein
745 kinase in Chlamydomonas reinhardtii. *PloS One* **8**:e69902.
746 doi:10.1371/journal.pone.0069902
747 Liang Y, Pang Y, Wu Q, Hu Z, Han X, Xu Y, Deng H, Pan J. 2014. FLA8/KIF3B
748 phosphorylation regulates kinesin-II interaction with IFT-B to control IFT entry
749 and turnaround. *Dev Cell* **30**:585–597. doi:10.1016/j.devcel.2014.07.019
750 Liang Y, Zhu X, Wu Q, Pan J. 2018. Ciliary Length Sensing Regulates IFT Entry via
751 Changes in FLA8/KIF3B Phosphorylation to Control Ciliary Assembly. *Curr Biol*
752 **28**:2429-2435.e3. doi:10.1016/j.cub.2018.05.069
753 Ludington WB, Ishikawa H, Serebrenik YV, Ritter A, Hernandez-Lopez RA,
754 Gunzenhauser J, Kannegaard E, Marshall WF. 2015. A systematic comparison
755 of mathematical models for inherent measurement of ciliary length: how a cell
756 can measure length and volume. *Biophys J* **108**:1361–1379.
757 doi:10.1016/j.bpj.2014.12.051
758 Ludington WB, Wemmer KA, Lechtreck KF, Witman GB, Marshall WF. 2013.
759 Avalanche-like behavior in ciliary import. *Proc Natl Acad Sci U S A* **110**:3925–
760 3930. doi:10.1073/pnas.1217354110
761 Mangeol P, Prevo B, Peterman EJG. 2016. KymographClear and KymographDirect: two
762 tools for the automated quantitative analysis of molecular and cellular dynamics
763 using kymographs. *Mol Biol Cell* **27**:1948–1957. doi:10.1091/mbc.E15-06-0404
764 Marshall WF, Qin H, Rodrigo Brenni M, Rosenbaum JL. 2005. Flagellar length control
765 system: testing a simple model based on intraflagellar transport and turnover.
766 *Mol Biol Cell* **16**:270–278. doi:10.1091/mbc.E04-07-0586
767 Matsuda A, Yoshimura K, Sineshchekov OA, Hirono M, Kamiya R. 1998. Isolation and
768 characterization of novel Chlamydomonas mutants that display phototaxis but not
769 photophobic response. *Cell Motil Cytoskeleton* **41**:353–362.
770 doi:10.1002/(SICI)1097-0169(1998)41:4<353::AID-CM7>3.0.CO;2-0
771 Mueller J, Perrone CA, Bower R, Cole DG, Porter ME. 2005. The FLA3 KAP subunit is
772 required for localization of kinesin-2 to the site of flagellar assembly and

773 processive anterograde intraflagellar transport. *Mol Biol Cell* **16**:1341–1354.
774 doi:10.1091/mbc.E04-10-0931
775 Nakai J, Ohkura M, Imoto K. 2001. A high signal-to-noise Ca(2+) probe composed of a
776 single green fluorescent protein. *Nat Biotechnol* **19**:137–141. doi:10.1038/84397
777 Nievergelt AP, Zykov I, Diener D, Chhatre A, Buchholz T-O, Delling M, Diez S, Jug F,
778 Štěpánek L, Pigino G. 2022. Conversion of anterograde into retrograde trains is
779 an intrinsic property of intraflagellar transport. *Curr Biol* **32**: 4071-4078.e4.
780 doi:10.1016/j.cub.2022.07.033
781 Pazour GJ, Agrin N, Leszyk J, Witman GB. 2005. Proteomic analysis of a eukaryotic
782 cilium. *J Cell Biol* **170**:103–113. doi:10.1083/jcb.200504008
783 Pigino G, Geimer S, Lanzavecchia S, Paccagnini E, Cantele F, Diener DR, Rosenbaum
784 JL, Lupetti P. 2009. Electron-tomographic analysis of intraflagellar transport
785 particle trains in situ. *J Cell Biol* **187**:135–148. doi:10.1083/jcb.200905103
786 Quader H, Cherniack J, Filner P. 1978. Participation of calcium in flagellar shortening
787 and regeneration in Chlamydomonas reinhardii. *Exp Cell Res* **113**:295–301.
788 Reck-Peterson SL, Redwine WB, Vale RD, Carter AP. 2018. The cytoplasmic dynein
789 transport machinery and its many cargoes. *Nat Rev Mol Cell Biol* **19**:382–398.
790 doi:10.1038/s41580-018-0004-3
791 Reiter JF, Leroux MR. 2017. Genes and molecular pathways underpinning ciliopathies.
792 *Nat Rev Mol Cell Biol* **18**:533–547. doi:10.1038/nrm.2017.60
793 Rosenbaum J. 2003. Organelle size regulation: length matters. *Curr Biol* **13**:R506-507.
794 Rosenbaum JL, Moulder JE, Ringo DL. 1969. Flagellar elongation and shortening in
795 Chlamydomonas. The use of cycloheximide and colchicine to study the synthesis
796 and assembly of flagellar proteins. *J Cell Biol* **41**:600–619.
797 Rosenbaum JL, Witman GB. 2002. Intraflagellar transport. *Nat Rev Mol Cell Biol* **3**:813–
798 825. doi:10.1038/nrm952
799 Rüffer U, Nultsch W. 1991. Flagellar photoresponses of Chlamydomonas cells held on
800 micropipettes: II. Change in flagellar beat pattern. *Cell Motil Cytoskeleton*
801 **18**:269–278. doi:10.1002/cm.970180404

802 Rupp G, Porter ME. 2003. A subunit of the dynein regulatory complex in
803 Chlamydomonas is a homologue of a growth arrest-specific gene product. *J Cell*
804 *Biol* **162**:47–57. doi:10.1083/jcb.200303019
805 Tuxhorn J, Daise T, Dentler WL. 1998. Regulation of flagellar length in
806 Chlamydomonas. *Cell Motil Cytoskeleton* **40**:133–146. doi:10.1002/(SICI)1097-
807 0169(1998)40:2<133::AID-CM3>3.0.CO;2-G
808 Wakabayashi K, Kamiya R. 2015. Axonemal motility in Chlamydomonas. *Methods Cell*
809 *Biol* **127**:387–402. doi:10.1016/bs.mcb.2014.12.002
810 Wang Y, Huynh W, Skokan TD, Lu W, Weiss A, Vale RD. 2019. CRACR2a is a calcium-
811 activated dynein adaptor protein that regulates endocytic traffic. *J Cell Biol*
812 **218**:1619–1633. doi:10.1083/jcb.201806097
813 Wemmer K, Ludington W, Marshall WF. 2020. Testing the role of intraflagellar transport
814 in flagellar length control using length-altering mutants of Chlamydomonas.
815 *Philos Trans R Soc Lond B Biol Sci* **375**:20190159. doi:10.1098/rstb.2019.0159
816 Wingfield JL, Mengoni I, Bomberger H, Jiang Y-Y, Walsh JD, Brown JM, Picariello T,
817 Cochran DA, Zhu B, Pan J, Eggenschwiler J, Gaertig J, Witman GB, Kner P,
818 Lechtreck K. 2017. IFT trains in different stages of assembly queue at the ciliary
819 base for consecutive release into the cilium. *eLife* **6**:e26609.
820 doi:10.7554/eLife.26609
821 Wullschleger S, Loewith R, Hall MN. 2006. TOR signaling in growth and metabolism.
822 *Cell* **124**:471–484. doi:10.1016/j.cell.2006.01.016
823 Yuan S, Li J, Diener DR, Choma MA, Rosenbaum JL, Sun Z. 2012. Target-of-
824 rapamycin complex 1 (Torc1) signaling modulates cilia size and function through
825 protein synthesis regulation. *Proc Natl Acad Sci U S A* **109**:2021–2026.
826 doi:10.1073/pnas.1112834109
827

828 **Figure legends**

829

830 **Figure 1** Schematic diagram and modeling of the ion-current model.

831 (A) The ion-current model assumes the ion channels are uniformly distributed along the
832 length of the flagellum, and Ca^{2+} ions entering the flagellum are proportional to the
833 flagellar length. Flagellar Ca^{2+} is assumed to negatively regulate IFT injection into flagella
834 to control the flagellar length. The longer flagellum can intake more ions, and these ions
835 inhibit IFT injection such that the further assembly of flagella is suppressed. (B) The
836 schema of kinesin-2 inactivation by Ca^{2+} and CDPK1 based on Liang et al. (2014). In a
837 Ca^{2+}-dependent manner, CDPK1 phosphorylates FLA8, a subunit of heterotrimeric
838 kinesin-2. Phosphorylated kinesin-2 loses its IFT protein binding activity. (C, D) Simulated
839 result of the ion-current model based on kinesin-2 phosphorylation by CDPK1 (Liang et
840 al., 2014), as detailed in Materials and methods. Flagellar length (C) and the ratio of
841 phosphorylated kinesin (D) were plotted against time.

842

843 **Figure 2** DRC4-GCaMP quantitatively detects free Ca^{2+}.

844 (A) Bright-field and fluorescent images of DRC4-GCaMP cells. DRC4-GCaMP localizes
845 to the entire length of flagella. Scale bar: 10 μm. (B) Fluorescent images of isolated DRC4-
846 mCherry-GCaMP axonemes. Axonemes were isolated from DRC4-mCherry-GCaMP
847 cells and were treated with various concentration of free Ca^{2+}. GCaMP intensity increased
848 as free Ca^{2+} concentration increased. Scale bar: 10 μm. (C) Semilogarithmic plot of
849 GCaMP and mCherry intensities. GCaMP and mCherry intensities were measured and
850 plotted. The blue dashed line shows the equation of a sigmoidal curve which is calculated
851 from the data.

852

853 **Figure 3** Quantification of Ca2+ influx as a function of flagellar length.

854 (A) Representative DRC4-GCaMP kymographs of *Chlamydomonas* flagella in control
855 (*pf2* DRC4-GCaMP), *ppr2* mutant (*pf2 ppr2* DRC4-GCaMP), 1 mM EGTA treated (*pf2*
856 DRC4-GCaMP), and 1 mM $CaCl_2$ treated (*pf2* DRC4-GCaMP) cells. These kymographs
857 were assembled from Videos 1-4. Horizontal bar: 5 s; vertical bar: 5 μm. (B) The intensity

858 of Ca^{2+} influx into flagella was calculated from kymographs and plotted against flagellar
859 length. Different lengths of flagella were obtained by imaging flagella during regeneration.
860 Control (blue circles, n = 272, Pearson correlation coefficient ρ = 0.21, and coefficient of
861 determination r^2 = 0.04), the *ppr2* mutant (red squares, n = 182, ρ = 0.14, and r^2 = 0.02),
862 and 1 mM $CaCl_2$ treated cells (green diamonds, n = 96, ρ = 0.46, and r^2 = 0.21). (C) The
863 frequency of Ca^{2+} influx was plotted against flagellar length. No obvious correlation was
864 detected in either the control (blue circles, ρ = 0.11, and r^2 = 0.01) or the *ppr2* mutant (red
865 squares, ρ = 0.004, and $r^2 = 1.85 \times 10^{-5}$). However, the frequency of Ca^{2+} influx in 1 mM
866 $CaCl_2$ treated cells was correlated with flagellar length (green diamonds, ρ = 0.33, and r^2
867 = 0.11). (D) The mean differences of Ca^{2+} influx intensity from the control regression line.
868 Data were plotted as scatter dot plots with mean ± SD. Statistical significance was
869 determined by an unpaired two-tailed t test against the control (**** P < 0.0001).
870
871 **Figure 4** Quantification of IFT injection as a function of flagellar length.
872 (A) Representative KAP-GFP kymographs of *Chlamydomonas* flagella in control (*fla3*
873 KAP-GFP), *ppr2* mutant (*fla3 ppr2* KAP-GFP), 1 mM EGTA treated (*fla3* KAP-GFP), and
874 1 mM $CaCl_2$ treated (*fla3* KAP-GFP) cells. These kymographs were assembled from
875 Videos 5-8. Horizontal bar: 5 s; vertical bar: 5 μm. (B) The mean KAP-GFP intensity of
876 each flagellum was calculated from kymographs and plotted against flagellar length.
877 Control (blue circles, n = 220, ρ = -0.72, and r^2 = 0.51), *ppr2* (red squares, n = 192, ρ = -
878 0.52, and r^2 = 0.27), EGTA (orange triangles, n = 162, ρ = -0.53, and r^2 = 0.28), and $CaCl_2$
879 (green diamonds, n = 116, ρ = -0.52, and r^2 = 0.27). (C) The mean difference of IFT
880 intensity from the control regression line. Data were plotted as scatter dot plot with mean
881 ± SD. Statistical significance was determined by an unpaired two-tailed t test against the
882 control (*** P < 0.001; **** P < 0.0001). (D) The frequency of KAP-GFP was plotted
883 against flagellar length. Control (blue circles, ρ = 0.17, and r^2 = 0.03), *ppr2* (red squares,
884 ρ = 0.51, and r^2 = 0.26), EGTA (orange triangles, ρ = 0.14, and r^2 = 0.02), and $CaCl_2$
885 (green diamonds, ρ = 0.38, and r^2 = 0.15). (E) The velocity of KAP-GFP was plotted
886 against flagellar length. Control (blue circles, ρ = 0.64, and r^2 = 0.41), *ppr2* (red squares,

887 ρ = 0.81, and r^2 = 0.64), EGTA (orange triangles, ρ = 0.69, and r^2 = 0.47), and $CaCl_2$
888 (green diamonds, ρ = 0.69, and r^2 = 0.48).
889
890 **Figure 5** The kinetics of flagellar regeneration and disassembly.
891 (A) Flagella were removed by the pH shock method. Mean flagellar length of control (wild-
892 type CC-125, blue circles), *ppr2* mutant (red squares), 1 mM EGTA treated (orange
893 triangle), and 1 mM $CaCl_2$ treated (green diamonds) cells was plotted against time after
894 pH shock. (B) The *fla10* mutant strains were transferred to the restrictive temperature
895 (33ºC). Mean flagellar length of control (*fla10*, blue circles), *fla10 ppr2* mutant (red
896 triangle), 1 mM EGTA treated *fla10* (orange diamonds), and 1 mM EGTA treated *fla10*
897 *ppr2* (magenta inverted triangles) cells was plotted against time after temperature shift.
898 20 biflagellated cells were measured per strain and time point.
899
900 **Figure 6** Dual-channel imaging of DRC4-GCaMP and mScarlet-IFT54.
901 (A) Representative kymographs and quantified data. The DRC4-GCaMP kymograph (top)
902 was generated from Video 9. Quantified intensity of Ca^{2+} influx is shown at the bottom of
903 the kymograph. The mScarlet-IFT54 kymograph (middle) was generated from Video 9.
904 Quantified anterograde IFT injection is shown at the bottom of the kymograph. The
905 merged kymograph (bottom) of DRC4-GCaMP (green) and mScarlet-IFT54 (magenta).
906 Horizontal bar: 5 s; vertical bar: 5 μm. (B) The mScarlet-IFT54 intensity of each flagellum
907 was calculated from kymographs and plotted against flagellar length (n = 116, and
908 Pearson correlation coefficient ρ = -0.47). Non-linear regression is indicated by a solid
909 line (r^2 = 0.21). (C) The frequency of anterograde IFT was plotted against flagellar length
910 (ρ = 0.53 and r^2 = 0.28). (D) The velocity of anterograde IFT was plotted against flagellar
911 length (ρ = 0.76 and r^2 = 0.58). (E) The intensity of Ca^{2+} influx into flagella was calculated
912 from kymographs and plotted against flagellar length (ρ = 0.33 and r^2 = 0.11). (F) The
913 mean mScarlet-IFT54 intensity was plotted against the intensity of Ca^{2+} influx (ρ = -0.08
914 and r^2 = 0.007).
915
916 **Figure 7** Quantification of IFT behavior after Ca^{2+} influx.

917 (A) Overview of the short-time analysis of IFT behavior after a burst of Ca^{2+} influx using
918 dual-channel imaging. Analyzed areas were colored on the representative kymographs
919 of DRC4-GCaMP and mScarlet-IFT54. Intervals of each area are 5 s. Bursts of Ca^{2+}
920 influx were selected where no previous Ca^{2+} influx was observed for more than 10 s
921 before the Ca^{2+} influx. The "c" area was set at the start of the burst of Ca^{2+} influx. The
922 areas "a" and "b" were set to 10 s and 5 s before the burst of Ca^{2+} influx at the "c" area.
923 The areas "d" and "e" were set to 5 s and 10 s after the start of the Ca^{2+} influx, respectively.
924 Horizontal bar: 5 s; vertical bar: 5 μm. (B-G) IFT behaviors before and after the burst of
925 Ca^{2+} influx were plotted against each area (n = 29). (B) The intensity of IFT injection. (C)
926 The intensity of returning IFT. (D) The frequency of anterograde IFT. (E) The frequency
927 of retrograde IFT. (F) The speed of anterograde IFT. (G) The speed of anterograde IFT.
928 (H) The sum of the Ca^{2+} influx before and after the burst of Ca^{2+} influx. (I) The background
929 intensity of mScarlet-IFT54. Statistical significance between neighboring areas was
930 determined by a paired two-tailed t test (* $P < 0.05$; ** $P < 0.01$; *** $P < 0.001$; **** $P <$
931 0.0001).
932
933
934 **Supporting Information**
935
936 **Figure 3 - figure supplement 1**
937 Example DRC4-GCaMP kymographs of *Chlamydomonas* flagella (control, *pf2* DRC4-
938 GCaMP). The pair of Flagellum 1 and Flagellum 2 are flagella from the same cells. The
939 pattern of Ca^{2+} influx events varied from flagellum to flagellum and from time to time.
940 Horizontal bar: 5 s; vertical bar: 5 μm.
941
942 **Figure 3 - figure supplement 2**
943 Individual Ca^{2+} influx events are not independent. Histogram shows Ca^{2+} spikes
944 distribution every 5 s. Blue line shows the DRC4-GCaMP (control) data from Figure 3.
945 Red dashed line shows calculated data to fit with Poisson distribution. Blue line does not

946 fit with red line (Chi-square goodness-of-fit test, $p < 0.0001$). Similar results were obtained
947 at other time intervals.
948
949 **Figure 5 - figure supplement 1**
950 Flagellar length of potential flagellar calcium pump mutant cells. Mutant strains, FAP10
951 and FAP39, were obtained from the CLiP library. The control cell is the background strain
952 of the library, CMJ030 (CC-4533 cw15 mt-). These mutations were identified from the
953 CLiP library database and not independently verified. 25 biflagellated cells were
954 measured per strain. All mutant strains showed no significant differences in flagellar
955 length from the control. Statistical significance was determined by an unpaired two-tailed
956 t test against the control.
957
958
959 **Figure 7 - figure supplement 1**
960 Additional examples of stalled IFT release by Ca^{2+} influx. Kymographs of DRC4-GCaMP
961 and mScarlet-IFT54 were from four different flagella. mScarlet-IFT54 was paused and
962 accumulated when Ca^{2+} influx was not observed for a long-time. These examples confirm
963 that Ca^{2+} influx can clear paused IFT for flagella. Horizontal bar: 5 s; vertical bar: 5 μm.
964
965
966 **Video 1**
967 Movie of DRC4-GCaMP in control (*pf2* DRC4-GCaMP) cell. This movie was taken at 20
968 frames per second (fps) and plays in real time.
969
970 **Video 2**
971 Movie of DRC4-GCaMP in the *ppr2* mutant (*pf2 ppr2* DRC4-GCaMP) cell. This movie
972 was taken at 20 fps and plays in real time.
973
974 **Video 3**

975 Movie of DRC4-GCaMP in 1 mM EGTA treated (*pf2* DRC4-GCaMP) cell. This movie was
976 taken at 20 fps and plays in real time.
977
978 **Video 4**
979 Movie of DRC4-GCaMP in 1 mM $CaCl_2$ treated (*pf2* DRC4-GCaMP) cell. This movie was
980 taken at 20 fps and plays in real time.
981
982 **Video 5**
983 Movie of KAP-GFP in control (*fla3* KAP-GFP) cell. This movie was taken at 20 fps and
984 plays in real time.
985
986 **Video 6**
987 Movie of KAP-GFP in the *ppr2* mutant (*fla3 ppr2* KAP-GFP) cell. This movie was taken at
988 20 fps and plays in real time.
989
990 **Video 7**
991 Movie of KAP-GFP in 1 mM EGTA treated (*fla3* KAP-GFP) cell. This movie was taken at
992 20 fps and plays in real time.
993
994 **Video 8**
995 Movie of KAP-GFP in 1 mM $CaCl_2$ treated (*fla3* KAP-GFP) cell. This movie was taken at
996 20 fps and plays in real time.
997
998 **Video 9**
999 Movie of DRC4-GCaMP and mScarlet-IFT54 in the *pf2 ift54* DRC4-GCaMP mScarlet-
1000 IFT54 cell. DRC4-GCaMP is shown in green, and mScarlet-IFT54 is shown in magenta.
1001 This movie was taken at 10 fps and plays in real time.
1002
1003

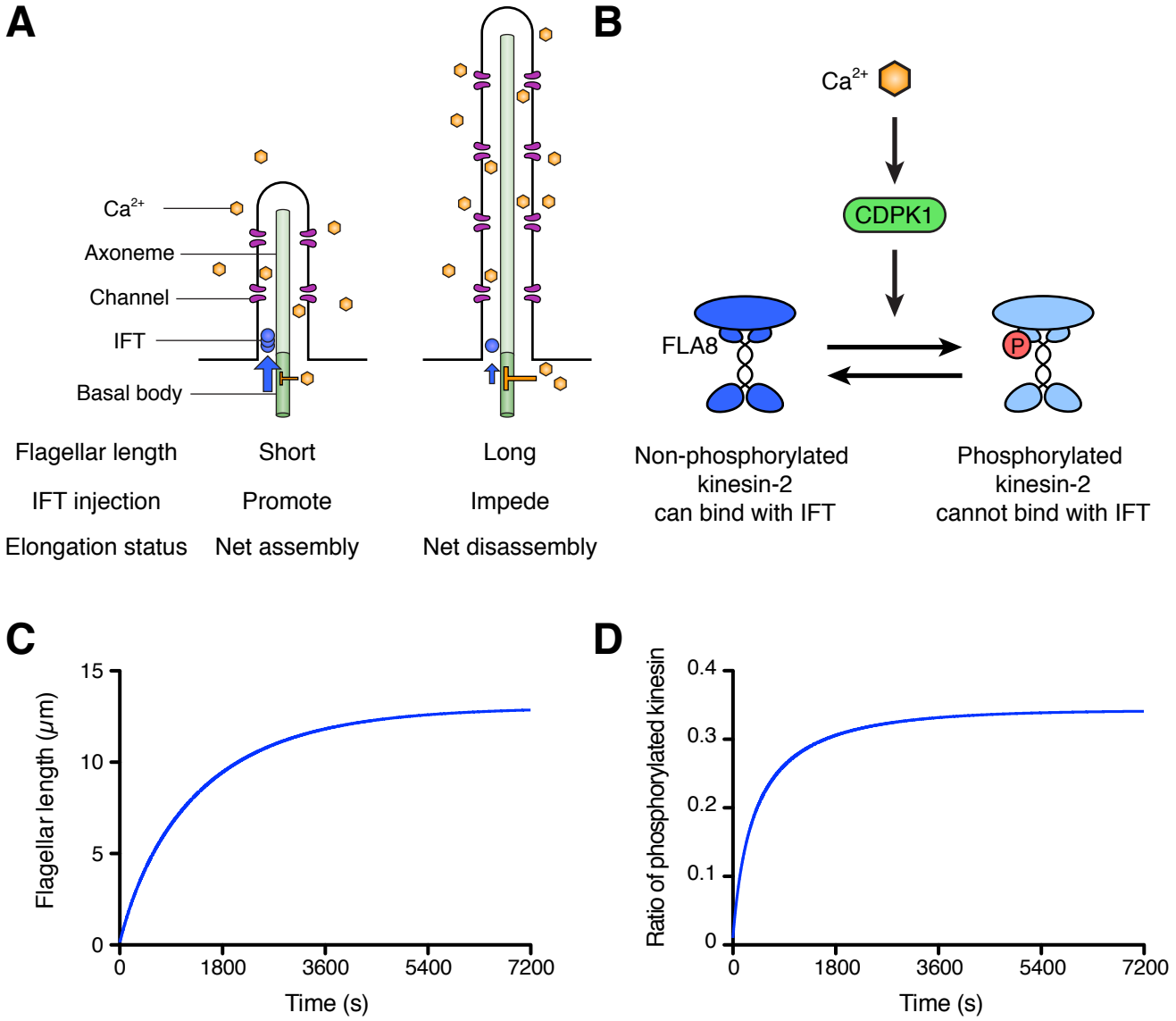
A
Ca2+
Axoneme
Channel
IFT
Basal body
Flagellar length
IFT injection
Elongation status
Short
Promote
Net assembly
Long
Impede
Net disassembly
B
Ca2+
CDPK1
FLA8
P
Non-phosphorylated kinesin-2 can bind with IFT
Phosphorylated kinesin-2 cannot bind with IFT
C
Flagellar length (μm)
15
10
5
0
0
1800
3600
5400
7200
Time (s)
D
Ratio of phosphorylated kinesin
0.4
0.3
0.2
0.1
0
0
1800
3600
5400
7200
Time (s)

Figure 1

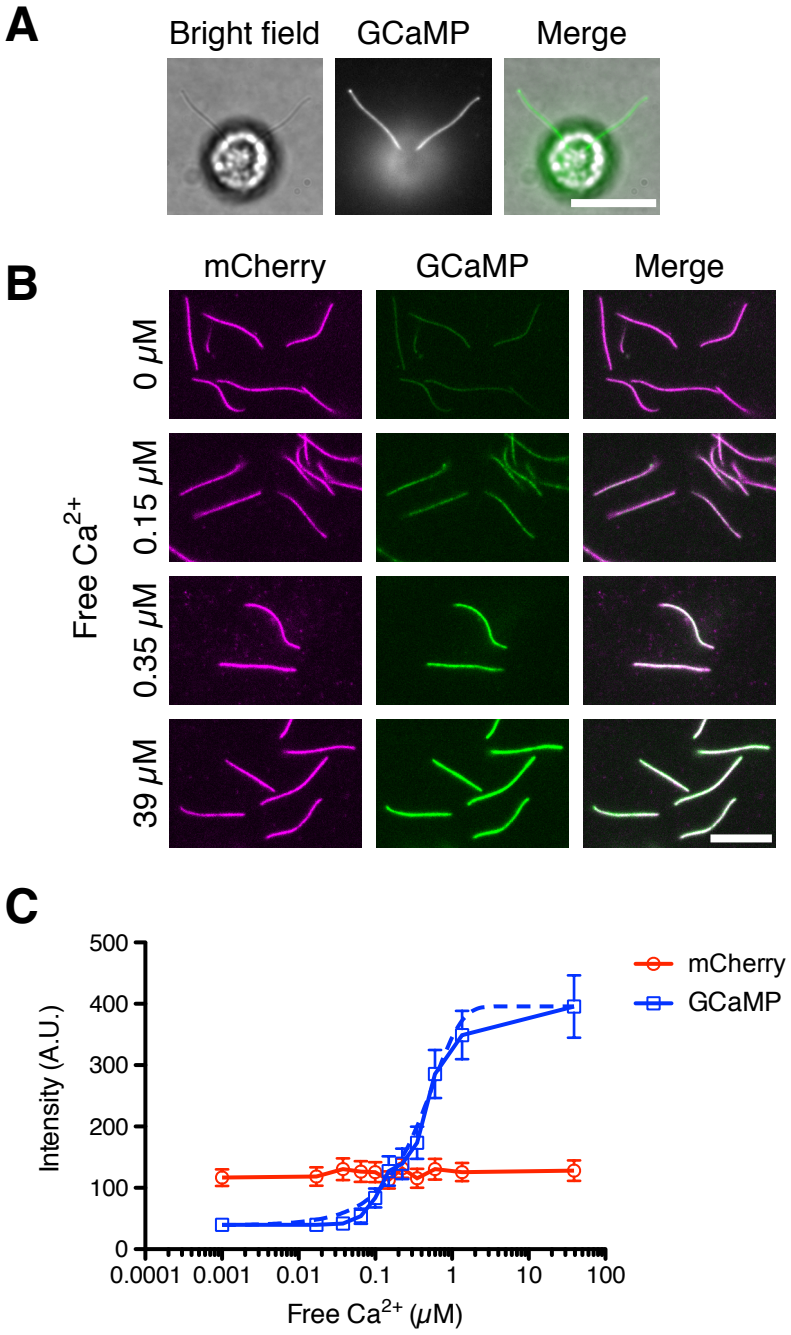
A
Bright field
GCaMP
Merge
B
mCherry
GCaMP
Merge
Free Ca2+
0 μM
0.15 μM
0.35 μM
39 μM
C
Intensity (A.U.)
500
400
300
200
100
0
0.0001
0.001
0.01
0.1
1
10
100
Free Ca2+ (μM)
mCherry
GCaMP

Figure 2

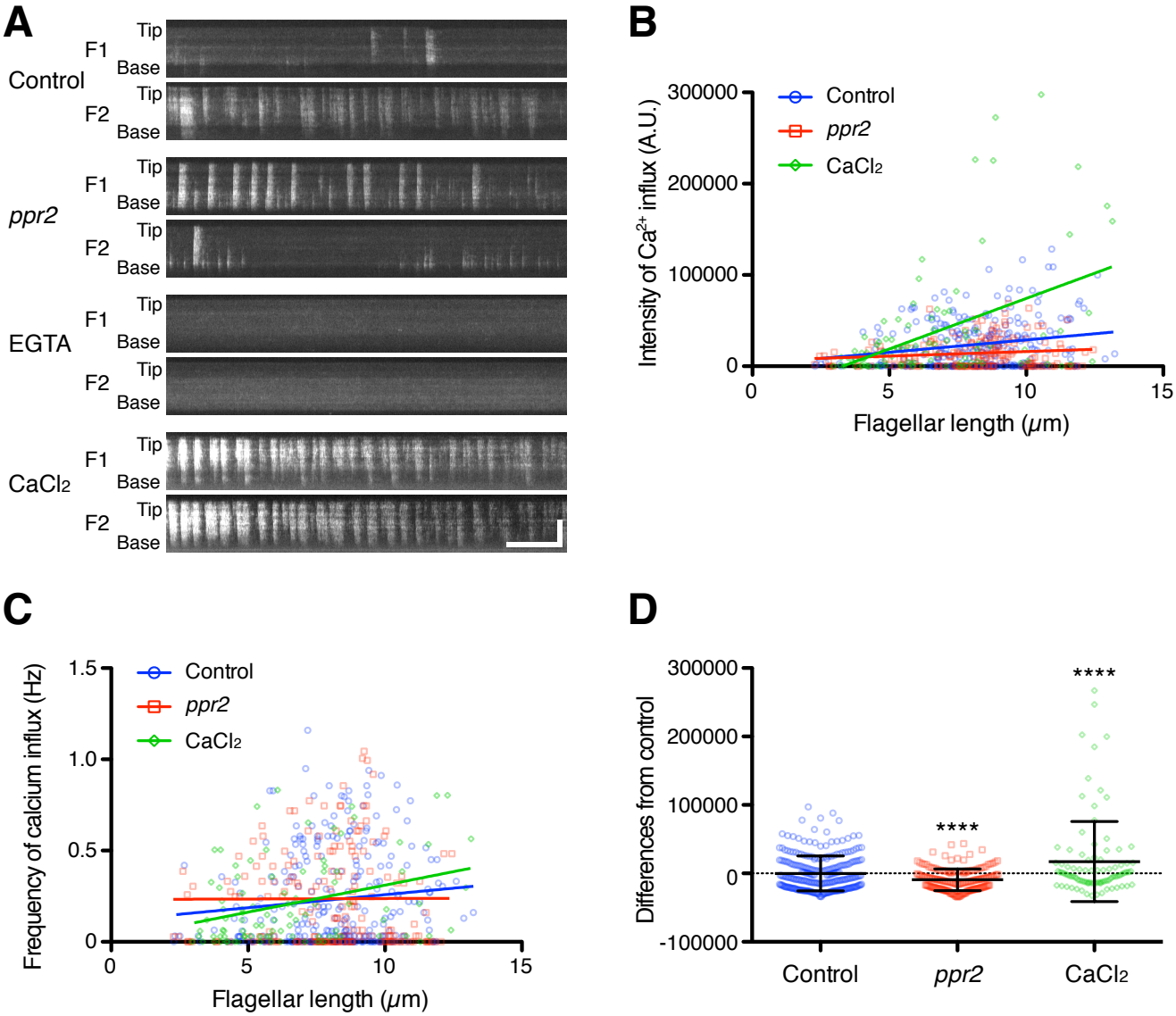
A
Control
F1
Tip
Base
F2
Tip
Base
ppr2
F1
Tip
Base
F2
Tip
Base
EGTA
F1
Tip
Base
F2
Tip
Base
CaCl2
F1
Tip
Base
F2
Tip
Base
B
Intensity of Ca2+ influx (A.U.)
300000
200000
100000
0
0
5
10
15
Flagellar length (μm)
Control
ppr2
CaCl2
C
Frequency of calcium influx (Hz)
1.5
1.0
0.5
0
0
5
10
15
Flagellar length (μm)
Control
ppr2
CaCl2
D
Differences from control
300000
200000
100000
0
-100000
****
****
Control
ppr2
CaCl2

Figure 3

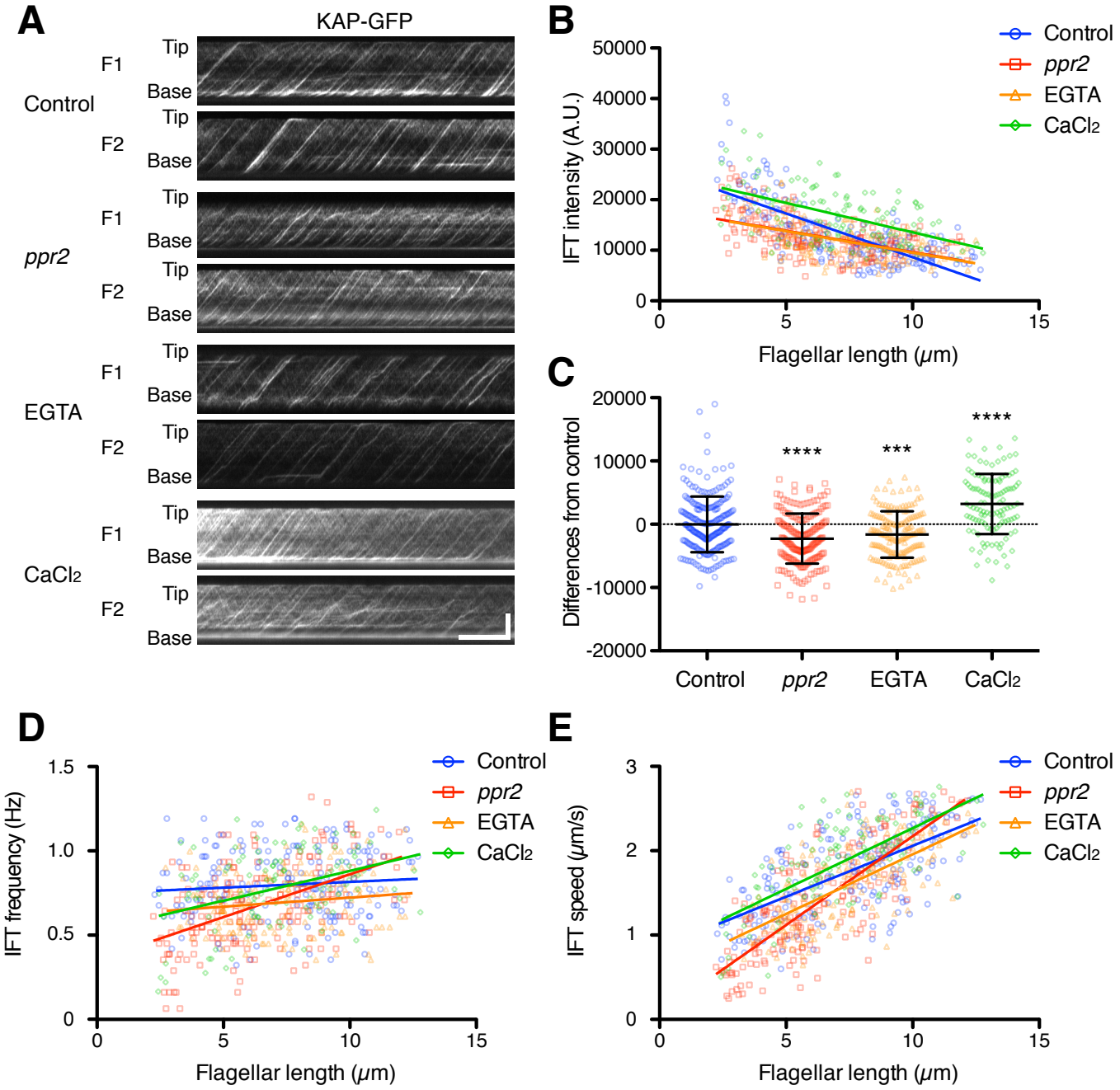
A
KAP-GFP
Control
F1
Tip
Base
F2
ppr2
EGTA
CaCl2
B
IFT intensity (A.U.)
Flagellar length (μm)
Control
ppr2
EGTA
CaCl2
C
Differences from control
****
***
****
Control
ppr2
EGTA
CaCl2
D
IFT frequency (Hz)
Flagellar length (μm)
E
IFT speed (μm/s)
Flagellar length (μm)

Figure 4

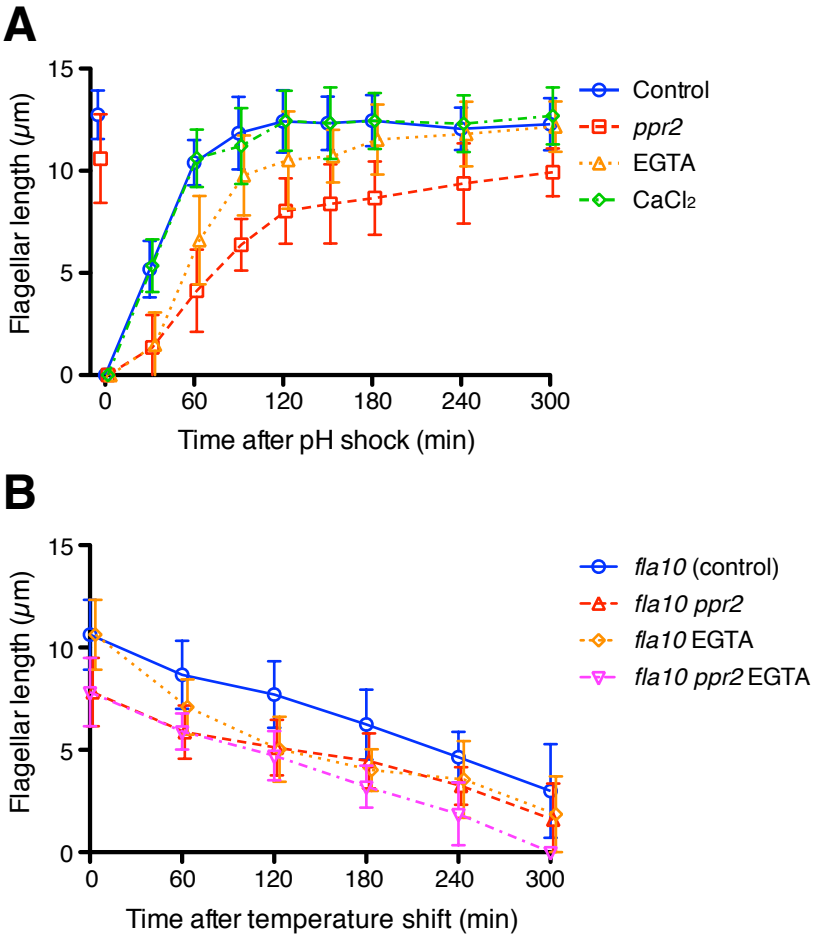
A
Flagellar length (μm)
15
10
5
0
0
60
120
180
240
300
Time after pH shock (min)
Control
ppr2
EGTA
CaCl2
B
Flagellar length (μm)
15
10
5
0
0
60
120
180
240
300
Time after temperature shift (min)
fla10 (control)
fla10 ppr2
fla10 EGTA
fla10 ppr2 EGTA

Figure 5

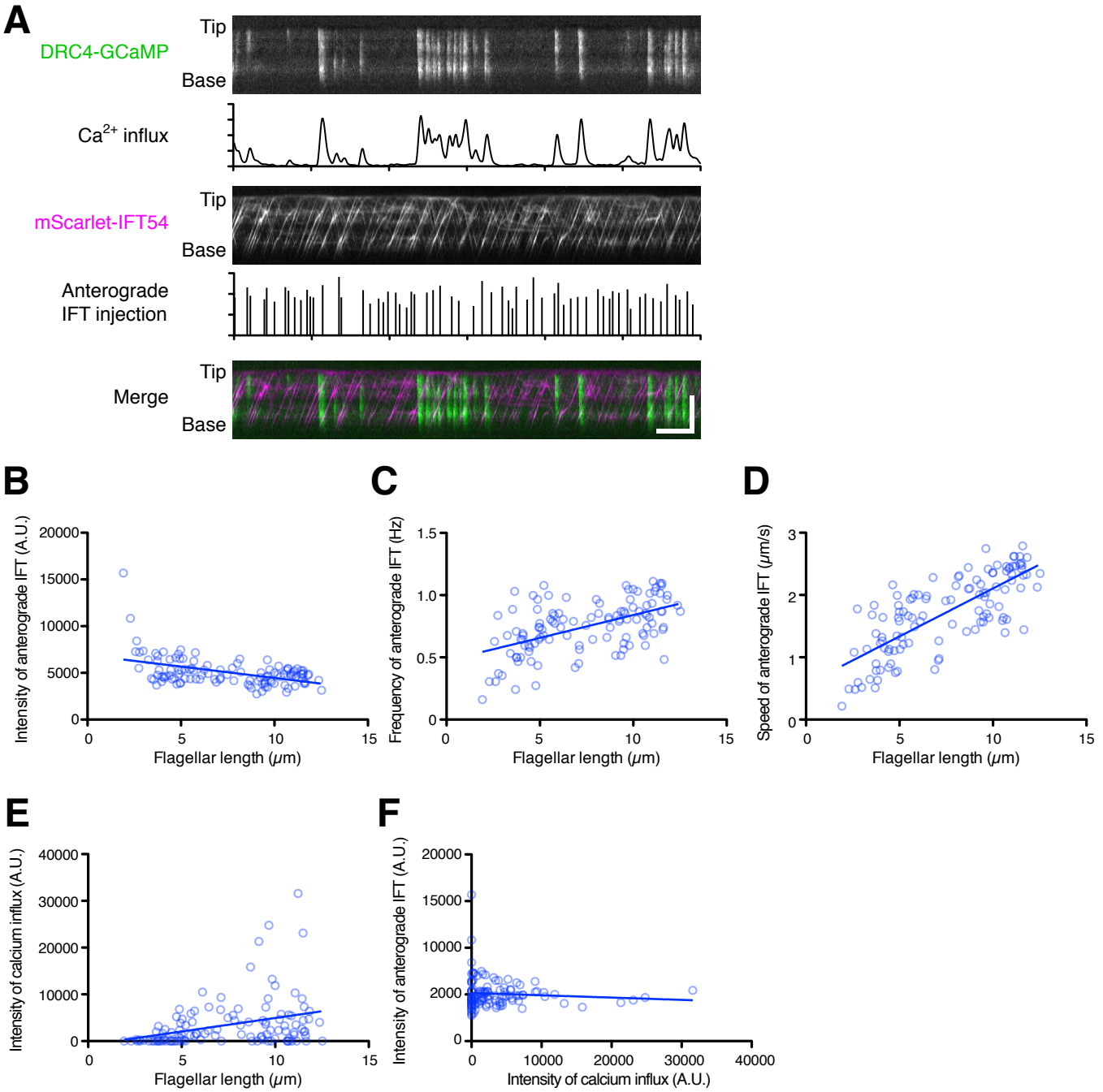
A
DRC4-GCaMP
Tip
Base
Ca2+ influx
mScarlet-IFT54
Tip
Base
Anterograde
IFT injection
Merge
Tip
Base
B
Intensity of anterograde IFT (A.U.)
Flagellar length (μm)
C
Frequency of anterograde IFT (Hz)
Flagellar length (μm)
D
Speed of anterograde IFT (μm/s)
Flagellar length (μm)
E
Intensity of calcium influx (A.U.)
Flagellar length (μm)
F
Intensity of anterograde IFT (A.U.)
Intensity of calcium influx (A.U.)

Figure 6

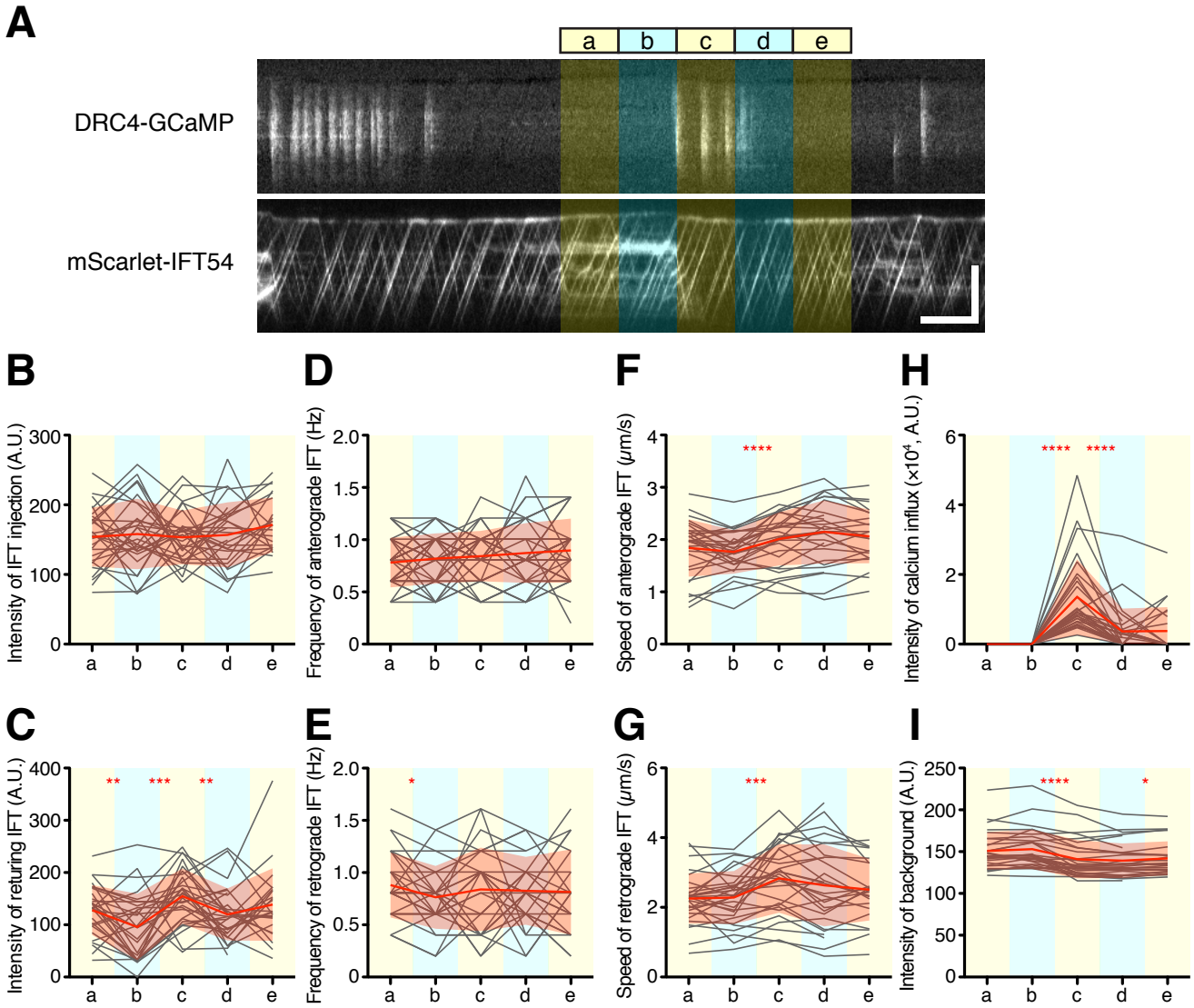
A
a
b
c
d
e
DRC4-GCaMP
mScarlet-IFT54
B
Intensity of IFT injection (A.U.)
C
Intensity of returing IFT (A.U.)
D
Frequency of anterograde IFT (Hz)
E
Frequency of retrograde IFT (Hz)
F
Speed of anterograde IFT (μm/s)
G
Speed of retrograde IFT (μm/s)
H
Intensity of calcium influx (x10⁴, A.U.)
I
Intensity of background (A.U.)

Figure 7

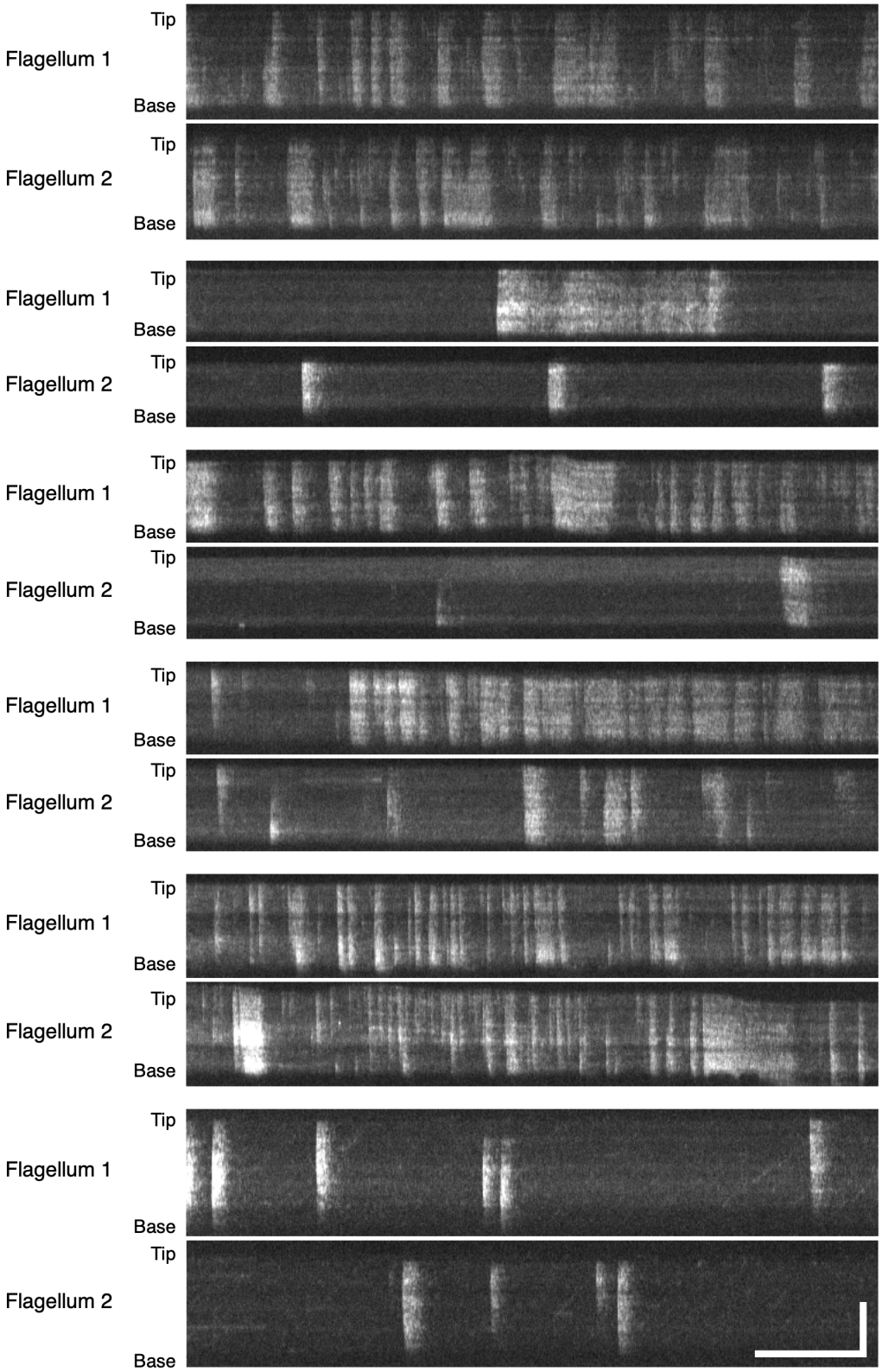
Flagellum 1
Tip
Base
Flagellum 2
Tip
Base
Flagellum 1
Tip
Base
Flagellum 2
Tip
Base
Flagellum 1
Tip
Base
Flagellum 2
Tip
Base
Flagellum 1
Tip
Base
Flagellum 2
Tip
Base
Flagellum 1
Tip
Base
Flagellum 2
Tip
Base

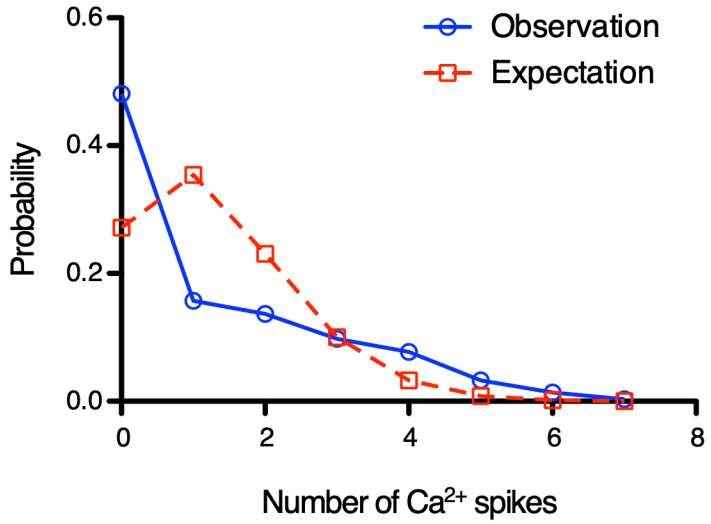
Observation
Expectation
Probability
0.6
0.4
0.2
0.0
0
2
4
6
8
Number of Ca2+ spikes

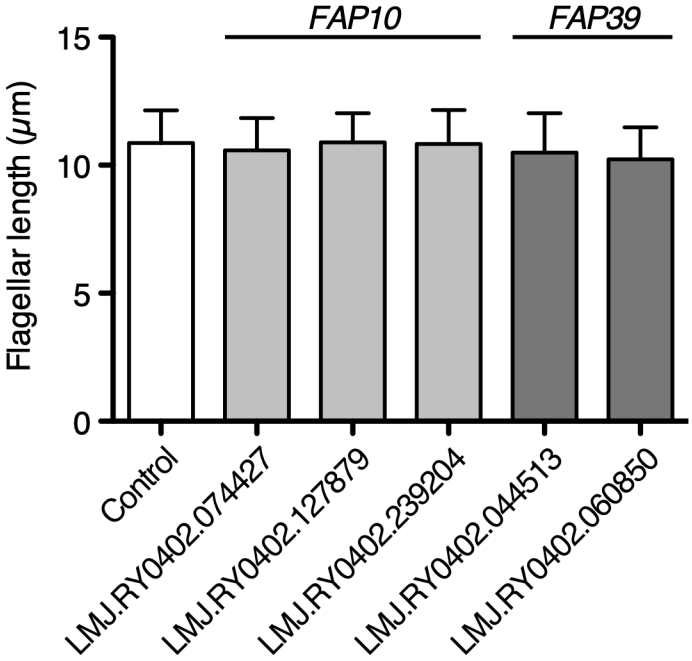
FAP10
FAP39
15
10
5
0
Flagellar length (μm)
Control
LMJ.RY0402.074427
LMJ.RY0402.127879
LMJ.RY0402.239204
LMJ.RY0402.044513
LMJ.RY0402.060850

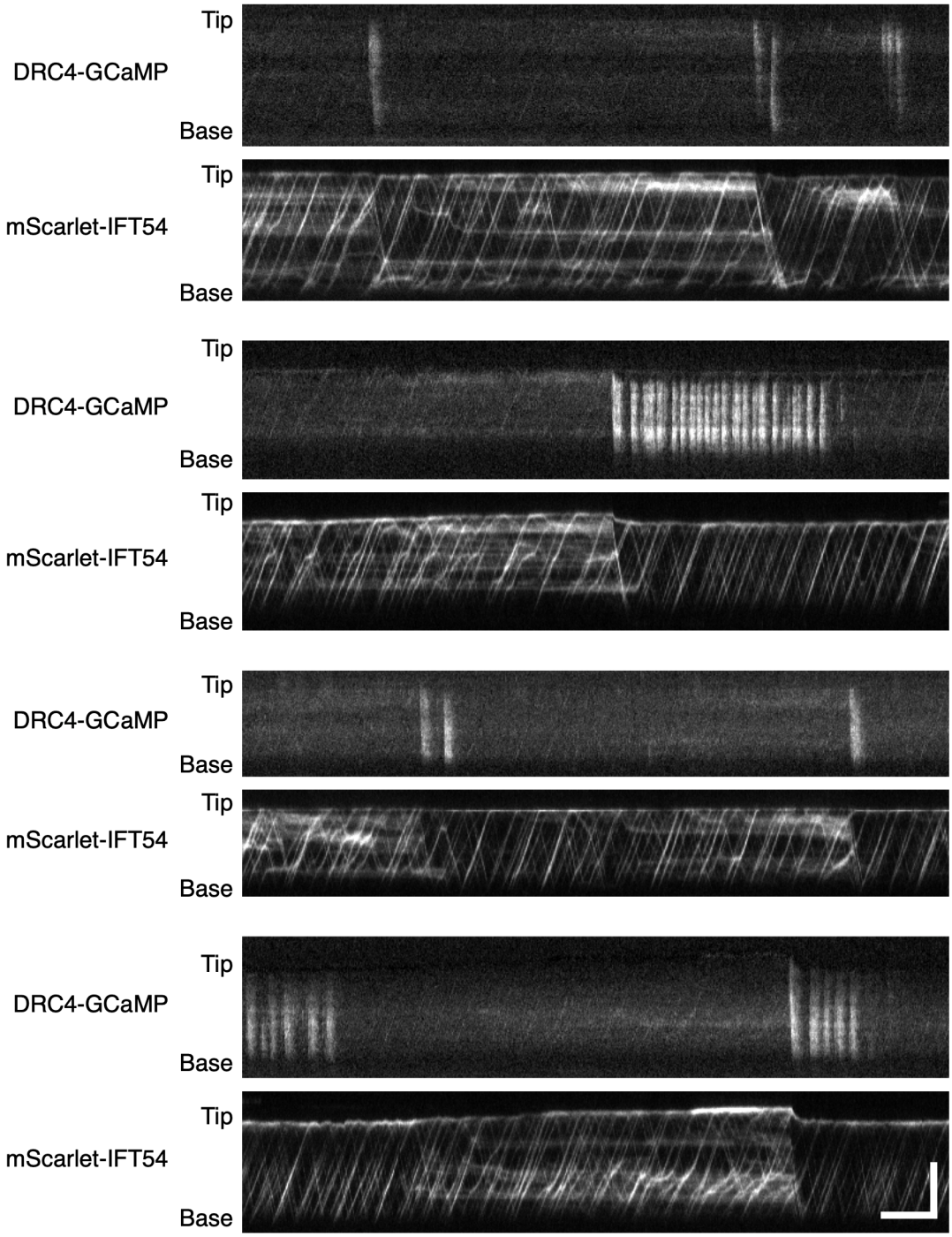
Tip
DRC4-GCaMP
Base
Tip
mScarlet-IFT54
Base
Tip
DRC4-GCaMP
Base
Tip
mScarlet-IFT54
Base
Tip
DRC4-GCaMP
Base
Tip
mScarlet-IFT54
Base
Tip
DRC4-GCaMP
Base
Tip
mScarlet-IFT54
Base